Mathematisch-Naturwissenschaftliche Fakultät

Yu Morishita | Milan Lazecky | Tim J. Wright | Jonathan R. Weiss |
John R. Elliott | Andy Hooper

LiCSBAS

An Open-Source InSAR Time Series Analysis Package Integrated with the
LiCSAR Automated Sentinel-1 InSAR Processor

LiCSBAS: An Open-Source InSAR Time Series Analysis Package Integrated with the LiCSAR Automated Sentinel-1 InSAR Processor

Yu Morishita [1,2,*] , **Milan Lazecky** [1] , **Tim J. Wright** [1] , **Jonathan R. Weiss** [1,3] , **John R. Elliott** [1] **and Andy Hooper** [1]

1   COMET, School of Earth and Environment, University of Leeds, Leeds LS2 9JT, UK;
     M.Lazecky@leeds.ac.uk (M.L.); T.J.Wright@leeds.ac.uk (T.J.W.); jonathan.weiss@uni-potsdam.de (J.R.W.);
     J.Elliott@leeds.ac.uk (J.R.E.); A.Hooper@leeds.ac.uk (A.H.)
2   Geography and Crustal Dynamics Research Center, Geospatial Information Authority of Japan,
     Tsukuba 305-0811, Japan
3   Institute of Geosciences, University of Potsdam, 14476 Potsdam, Germany
*   Correspondence: morishita-y96pt@mlit.go.jp

Abstract: For the past five years, the 2-satellite Sentinel-1 constellation has provided abundant and useful Synthetic Aperture Radar (SAR) data, which have the potential to reveal global ground surface deformation at high spatial and temporal resolutions. However, for most users, fully exploiting the large amount of associated data is challenging, especially over wide areas. To help address this challenge, we have developed LiCSBAS, an open-source SAR interferometry (InSAR) time series analysis package that integrates with the automated Sentinel-1 InSAR processor (LiCSAR). LiCSBAS utilizes freely available LiCSAR products, and users can save processing time and disk space while obtaining the results of InSAR time series analysis. In the LiCSBAS processing scheme, interferograms with many unwrapping errors are automatically identified by loop closure and removed. Reliable time series and velocities are derived with the aid of masking using several noise indices. The easy implementation of atmospheric corrections to reduce noise is achieved with the Generic Atmospheric Correction Online Service for InSAR (GACOS). Using case studies in southern Tohoku and the Echigo Plain, Japan, we demonstrate that LiCSBAS applied to LiCSAR products can detect both large-scale (>100 km) and localized (~km) relative displacements with an accuracy of <1 cm/epoch and ~2 mm/yr. We detect displacements with different temporal characteristics, including linear, periodic, and episodic, in Niigata, Ojiya, and Sanjo City, respectively. LiCSBAS and LiCSAR products facilitate greater exploitation of globally available and abundant SAR datasets and enhance their applications for scientific research and societal benefit.

Keywords: InSAR; Sentinel-1; time series analysis; deformation monitoring; tectonics; subsidence; automatic processing; global

1. Introduction

Synthetic aperture radar interferometry (InSAR) has been widely used to measure ground surface deformation with high spatial resolution (e.g., [1,2]). In particular, InSAR time series analysis, which utilizes a stack of SAR images, enables the detection of slow (~mm/yr) and/or time-variable deformation [3,4]. Until the mid-2010s, despite many successful applications of time series analysis across small areas (~10s km) (e.g., [1,5–8]), applicable regions were still limited due to inhomogeneous data availability, low observation frequency, data access policies, and variable coherence [2]. Measuring

large-scale tectonic deformation was also challenging (e.g., [9,10]) due, in part, to typical swath widths of up to ~100 km for image mode data, such as those provided by ASAR on ENVISAT.

The dual-satellite Sentinel-1 constellation, operated by the European Space Agency (ESA) as part of the European Commission's Copernicus Programme [11], has drastically changed the situation and outlook for the systematic exploitation of SAR data. Sentinel-1 routinely and frequently (every 6 or 12 days, depending on the area) acquires data over all the onshore areas on Earth, with ascending and descending information acquired in the tectonically straining regions [12]. The swath width of the Interferometric Wide Swath (IWS) mode is ~250 km, which is suitable for large-scale tectonic deformation monitoring. The data are freely and openly distributed under the ESA Copernicus Initiative for Earth Observation.

Although data availability has been greatly improved by Sentinel-1, there are still hurdles to overcome for the full exploitation of this near-global coverage and the huge amount of associated data. If users start with the Single Look Complex (SLC) images (generated by ESA from the L0 raw data), they need tremendous amounts of disk space, computing resources, processing time, and extensive knowledge of InSAR techniques. Whilst several free software packages have been developed and are available for InSAR processing (e.g., GMTSAR [13,14], ISCE [15,16], SNAP [17]) and time series analysis (GIAnT [18,19], MintPy [20,21], and StaMPS [3,22]), they remain technically complex and can be challenging to use for nonexperts.

Some online services promote and facilitate the wider exploitation of Sentinel-1 InSAR products. For example, ESA's Geohazard Exploitation Platform (GEP) is a user-friendly web-based platform where users can run unsupervised InSAR time series analysis on ESA's Grid Processing On Demand (G-POD) environment [23,24]. Users do not need to have the hardware nor software to process the huge amount of Sentinel-1 data. Instead, to obtain a result from the time series analysis, they need only to set the area of interest, select the SAR images to be processed, and choose the processing parameters before submitting the jobs online. However, adjusting processing parameters and error handling is difficult, because GEP acts as a "black box". Furthermore, it is currently a beta prototype, and access to it is restricted to early adopters only.

NASA's Advanced Rapid Imaging and Analysis (ARIA) project provides Sentinel-1 InSAR beta-products, including geocoded unwrapped interferograms [25] and the post-processing data preparation tools [26,27] for the GIAnT [18,19] and MintPy [20,21] time series analysis packages. As of November 2019, ~45,000 ARIA interferograms are available, mostly limited to parts of the United States of America and China.

Looking inside the Continents from Space (LiCS) is one of the projects led by the United Kingdom Natural Environment Research Council's Centre for the Observation and Modelling of Earthquakes, Volcanoes and Tectonics (COMET). The aims of LiCS are to monitor global tectonic and volcanic zones using Sentinel-1 InSAR, to map tectonic strain at high spatial resolution, and to use the results to inform new models of seismic and volcanic hazards. LiCSAR, which is an automated Sentinel-1 InSAR processor that uses GAMMA SAR and Interferometry software [28,29], has been developed to meet the primary LiCS project goals. As of November 2019, ~160,000 interferograms have been produced, mainly covering the Alpine Himalayan Belt and global volcanoes, and are published on the COMET-LiCS web portal [30]. LiCS coverage is currently being expanded to a global scale for deforming regions.

We have recently developed an open-source InSAR time series analysis package (LiCSBAS) that integrates with LiCSAR [31]. LiCSBAS utilizes the LiCSAR products so that users do not need to produce interferograms from SLC data. Instead, LiCSBAS enables users to easily obtain InSAR time series and velocity estimates wherever sufficient LiCSAR products are available. These results can be used for a variety of purposes, ranging from large-scale tectonic to localized anthropogenic surface deformation studies.

This paper is organized as follows. Section 2 describes the LiCSAR products and LiCSBAS workflow. Sections 3 and 4 present Japan-focused case studies for large- and small-scale deformations,

including an evaluation of the time series and velocity uncertainties. In Section 5, we discuss the advantages and limitations of LiCSBAS prior to presenting some concluding remarks in Section 6.

2. LiCSAR and LiCSBAS

2.1. LiCSAR: Automatic Sentinel-1 InSAR Processer

In the LiCSAR processing chain, interferograms are automatically produced on a predefined LiCSAR frame basis (generally consisting of 13 bursts on each of the three subswaths for IWS mode corresponding to an area of 250 km × 250 km). Newly acquired data are coregistered to a single primary image with the support of an auxiliary secondary image (nearer in time to the latest image to preserve coherence) that has been already coregistered (if available) using the enhanced spectral diversity method [32,33]. Each acquisition is then used to produce interferograms, by default, with three preceding and three subsequent acquisitions, although this number might be increased in the future. The interferograms are multilooked, with a factor of 20 × 4 in range × azimuth (46 × 56 m spacing), respectively, and spatially filtered to reduce noise using a GAMMA adaptive power spectrum filter with an alpha value of 1.0 [34]. LiCSAR unwraps the phase in two dimensions using a statistical cost approach with the SNAPHU software [35,36]. During the phase unwrapping, decorrelated areas in the interferograms are masked where the phase noise coherence estimate of the filtered interferogram is < 0.5. Wrapped and unwrapped interferograms and coherence images are geocoded with a pixel spacing of 0.001 degree (~100 m) and converted to the GeoTIFF format. The GeoTIFF files and quick-look images are published on the COMET-LiCS Sentinel-1 InSAR portal web and available for free download [30]. Other metadata (e.g., line-of-sight (LOS) vectors and perpendicular baselines) are also available on the COMET-LiCS web portal.

Currently (as of November 2019), up-to-date LiCSAR products are available primarily over the Alpine Himalayan Belt, Japan, the East African Rift, and for global volcanoes, although coverage continues to be expanded. For more details about LiCSAR, please refer to Lazecky et al. [37].

2.2. LiCSBAS Overview

Here, we provide a brief LiCSBAS overview prior to the detailed description presented in Sections 2.3–2.5. The workflow of our InSAR time series processor is largely divided into two parts: preparation of a stack of unwrapped data (Step 0) and time series analysis (Step 1; Figure 1). LiCSBAS starts with downloading the LiCSAR products covering the area of interest (Step 0-1) and is followed by data format conversion (Step 0-2). Tropospheric noise correction using the external Generic Atmospheric Correction Online Service for InSAR (GACOS) data [38] (Step 0-3) and masking (Step 0-4)/clipping (Step 0-5) the unwrapped data are optional steps that can be carried out to improve accuracy and make processing more efficient. In the time series analysis, incorrectly unwrapped data, which degrade the results, are identified and discarded based on the coherence and coverage of the unwrapped data (Step 1-1) and by checking loop closure (Step 1-2). The refined stack of unwrapped data is inverted to obtain the displacement time series and velocity (Step 1-3), followed by estimation of the velocity standard deviation (STD) (Step 1-4) and masking of noisy pixels based on several noise indices (Step 1-5). Finally, a spatiotemporal filter is applied to the time series to mitigate the residual noise and derive the filtered time series and velocity (Step 1-6). All steps can be executed from the command line or using a batch script with defined parameters. The derived results (i.e., velocity and time series) can be easily displayed by an interactive time series viewer and exported to GeoTIFF, KMZ, or text format.

LiCSBAS is written in Python3 and the Bourne Again Shell (bash) and operates without relying on any commercial software. The source codes are available on GitHub [31]. Although Steps 0-1 and 0-2 are dedicated specifically to manipulating LiCSAR products, interferograms from satellites other than Sentinel-1 and generated using a variety of software packages can be processed from Step 0-3, assuming the required metadata are available and files are converted into a compatible format

(4-byte, single-precision floating-point format). Future LiCSBAS enhancements may include functions to prepare input data from InSAR archives other than LiCSAR (e.g., ARIA, etc.).

Figure 1. Workflow of LiCSBAS comprising the preparation of unwrapped (UNW) interferometric phases and coherence (COH) data (Steps 0-1 to 0-5) prior to the time series analysis (Steps 1-1 to 1-6). Optional steps of incorporating atmospheric corrections (Generic Atmospheric Correction Online Service, GACOS); masking; and clipping are denoted by the dashed lines. Checks are performed for poorly unwrapped interferograms prior to the small baseline (SB) inversion to generate velocities and time series. A range of noise indices are calculated to mask poorly constrained data points. Further masking and filtering occur to generate the final products.

2.3. Prepare Stack of Unwrapped Data

2.3.1. Step 0-1: Download LiCSAR Products

GeoTIFF files of unwrapped phase and coherence are published on the COMET-LiCS web portal [30] for the full frame mosaic (typically 250 × 250 km) covering all the ascending and descending data (which are treated independently). The GeoTIFF files for all the frames of a specified time period (normally this is to place 2014 to the earliest date to the latest, or present, date automatically) are downloaded in this step. Some available metadata (e.g., LOS unit vectors and perpendicular baselines) are also included in the download.

2.3.2. Step 0-2: Convert GeoTIFF (and Downsample)

The downloaded GeoTIFF files are converted to a single-precision floating-point format without header information for the following processing steps. Downsampling (i.e., multilooking) can also be applied if the full resolution of the LiCSAR products (~100 m) is not needed. Downsampling is achieved by boxcar averaging and returns null if more than half of the pixels in the boxcar window are null. Downsampling results in faster overall processing, a reduction in the file size, and is also useful for quickly testing processing parameters and making adjustments prior to running the processing at a full or higher resolution.

2.3.3. Step 0-3: Tropospheric Noise Correction Using GACOS (Optional)

2.3.3. Step 0-3: Tropospheric Noise Correction Using GACOS (Optional)

Interferograms are contaminated by phase noise from path delays due to spatially- and temporally-varying tropospheric water vapor, temperature, and pressure, which can reach 10 cm or more [39,40]. In standard time series analysis algorithms, spatiotemporal filtering (i.e., high-pass in time and low-pass in space) is used to separate spatially correlated noise from deformation signals under the assumption that the noise component is uncorrelated in time [3,5,7]. This option is also available in LiCSBAS (Step 1-6 explained in Section 2.4.6), but the assumption that noise is uncorrelated in time is not always correct. If the tropospheric delay is correlated in time and/or the deformation is uncorrelated in time, the deformation time series may be poorly recovered [41–43]. Furthermore, temporal filtering does not improve the accuracy of the average velocities retrieved from the time series. Mitigation of the tropospheric noise before the spatiotemporal filtering using independent data improves the accuracy of the derived displacement time series and the average velocities.

GACOS provides tropospheric delay maps derived from the high-resolution European Centre for Medium-Range Weather Forecasts (ECMWF) data [44] for correction of the tropospheric noise present in interferograms [38]. The GACOS corrections are globally available in near real-time, and users can request the delay maps for specific areas and times through a web application system [45] and download these corrections once they have been produced.

Step 0-3 applies the GACOS corrections to the stack of unwrapped interferograms. Currently, users need to separately prepare the GACOS data for the processing area and acquisition dates beforehand. However, a one-stop service for LiCSAR is being planned in which the GACOS data for all Sentinel-1 acquisitions will be provided along with the interferograms via the COMET-LiCS web portal.

This step is optional but recommended to improve the accuracy of the time series (see Section 3.4). However, since the GACOS corrections may have a negative impact in some cases [46,47], users should check if reasonable noise mitigation has been achieved after applying the corrections. LiCSBAS calculates the STD of unwrapped phases before and after the GACOS corrections and their reduction rates for each interferogram, as well as creates quick-look images of unwrapped interferograms before and after the correction and the correction itself to aid in checking the GACOS effects (Figure S1). In case the GACOS corrections have a negative impact, other methods (e.g., linear, power-law [40], or spatially varying scaling [48] methods for the topography-correlated component) could be useful and may be integrated in the future.

2.3.4. Step 0-4: Mask Interferograms (Optional)

This step masks specified rectangular areas (e.g., isolated islands) in the stack of unwrapped data (Figure S2), which is useful if these areas have unwrapping errors. Masking may improve the network refinement at Step 1-2 (see Sections 2.4.2 and 3.3).

2.3.5. Step 0-5: Clip Interferograms (Optional)

This step clips a specified rectangular area from the stack of unwrapped data (Figure S3). Clipping is recommended if the area of interest does not cover the entire frame, because it decreases the processing time and results in smaller file sizes (see Section 5.1). Note that a stable reference area should be included in the clipped area. Clipping may also improve network refinement in Step 1-2 by removing unnecessary areas where unwrapping errors might be present (see Section 4).

2.4. Time Series Analysis

2.4.1. Step 1-1: Quality Check

LiCSAR products may contain not only useful coherent interferograms but also severely decorrelated interferograms due to factors such as vegetation or snow cover that result in a very low percentage of valid unwrapped pixels (Figure S4a,b). Moreover, Sentinel-1 SLC data distributed by ESA do not always cover an entire LiCSAR frame (i.e., some bursts may be missing in a frame).

Interferograms derived from data with missing bursts may also have low coverage (Figure S4c), and these incomplete data with low coverage negatively impact LiCSBAS processing and should be flagged as bad data. In Step 1-1, the bad data are identified based on statistics including the average coherence and the percentage of valid unwrapped pixels.

2.4.2. Step 1-2: Network Refinement by Loop Closure

Unwrapped data may include unwrapping errors, which can cause significant errors in the derived time series and should therefore be removed or corrected beforehand. Several approaches have been proposed to identify and correct unwrapping errors, taking advantage of the redundancy of a network of interferograms and loop phase closure [21,49,50]. However, manual identification or correction is too time-consuming for a full stack of LiCSAR interferograms [49]. Automatic correction can work well only if the redundancy of the network of interferograms is sufficiently high and not too many unwrapping errors exist [21,50], which may not always be the case for large-scale, automatic processing. Moreover, automatic unwrapping error correction can produce false corrections, which are difficult to identify and result in worse errors in the derived time series. Therefore, for now, we have decided to take a conservative approach; we automatically detect and completely remove interferograms that have many unwrapping errors by evaluating the loop phase closure on an image-by-image basis, rather than correcting unwrapping errors on a pixel-by-pixel basis.

Supposing that we have three images (ϕ_1, ϕ_2, and ϕ_3) and three unwrapped interferograms (ϕ_{12}, ϕ_{23}, and ϕ_{13}), a loop phase (also called closure phase or phase triplet) is calculated by [49]

$$\Phi_{123} = \phi_{12} + \phi_{23} - \phi_{13}. \tag{1}$$

If there are no unwrapping errors in the three interferograms, the loop phase should be close to zero (but not exactly zero due to the effects of multilooking, filtering, soil moisture change, etc. [51]). On the other hand, if one (or more) of the interferograms contains unwrapping errors, the loop phase will usually be close to an integer multiple of 2π (Figure 2). The root mean square (RMS) of the loop phase image indicates how many pixels with unwrapping errors are included in the loop. All possible loop phases and the RMS are calculated, and problematic loops with larger RMS than a defined threshold (e.g., 1.5 rad) can be identified. If all loops associated with an interferogram are problematic, this is considered a bad interferogram that likely includes many unwrapping errors, and it is removed from further processing (Figure 2).

Note that this step evaluates unwrapping errors for each interferogram but not for each pixel. Interferograms that are removed during Step 1-2 may contain correctly unwrapped pixels. However, this is not a significant problem if sufficient interferograms still remain after network refinement. Conversely, remaining interferograms may still contain some unwrapping errors, which would degrade the derived time series. These errors generate unclosed loops on a pixel-by-pixel basis. We count the number of unclosed loops for each pixel and can use this for masking pixels with unwrapping errors after the small baseline (SB) inversion at Step 1-5 (Section 2.4.5).

If two interferograms in a loop have opposite unwrapping errors in the same area, the loop phase is falsely closed, and the bad interferograms may not be automatically identified. However, network redundancy assures that other loops associated with the unidentified bad interferograms are not closed and will be counted on a pixel-by-pixel basis and identified at the later masking step (Step 1-5, Section 2.4.5). Users can also manually identify and remove the unidentified bad interferograms by checking the loop closure images (Figure 2) and then re-run Step 1-2.

After network refinement, a preliminary reference point is selected. At the reference point, all interferograms must have valid (unmasked) and error-free unwrapped data for the following SB network inversion. To identify the reference point, the RMS of all the loop phases for each pixel is calculated, and the pixel with the smallest RMS is selected.
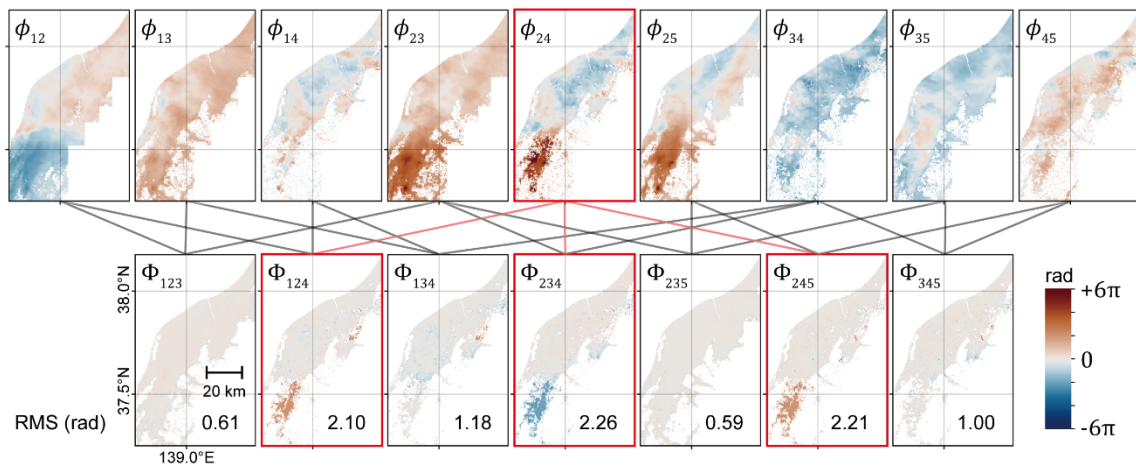
Figure 2. Example of the loop closure for the region of the Echigo plain, Japan (Section 4). Top and bottom row images are interferograms consisting of five images and loop phases calculated from the interferograms by Equation (1), respectively. Black and red lines between them denote which three interferograms are used to calculate each loop phase. Three loop phases with a red frame (Φ_{124}, Φ_{234}, Φ_{245}) have areas with $\pm 2\pi$ phase and a large (>2 rad) root mean square (RMS). Then, the interferogram ϕ_{24}, with a red frame, can be identified as a bad interferogram including significant unwrapping errors, because all loops associated with it are problematic, whilst the other interferograms generate at least one nonproblematic loop.

2.4.3. Step 1-3: Small Baseline Network Inversion

In order to perform an estimate of the velocity of a surface pixel through time based upon a series of displacement data, we perform an SB inversion on the network of interferograms. Suppose that we have a stack of M-unwrapped interferograms $\mathbf{d} = [d_1, \ldots, d_M]^T$ produced from N images acquired at $(t_0, \ldots, t_{N-1})$, N-1 incremental displacement vector $\mathbf{m} = [m_1, \ldots, m_{N-1}]^T$ (i.e., m_i is the incremental displacement between time t_{i-1} and t_i) can be derived by solving

$$\mathbf{d} = \mathbf{G}\mathbf{m} \tag{2}$$

where $\mathbf{G}$ is a $M \times (N$-1) design matrix of zeros and ones describing the relationship between the network of the interferograms and incremental displacements, considering that the unwrapped interferogram (i.e., displacement between two acquisitions) is the sum of corresponding successive incremental displacements [52]. Cumulative displacements for each acquisition (i.e., the displacement time series) are simply calculated by summing the incremental displacements. The mean displacement velocity is then derived from the cumulative displacements by least-squares.

Even though Sentinel-1 data are constantly being acquired with short spatial and temporal baselines in most areas (unlike with predecessors such as Envisat and ERS), there could still be gaps in the SB network (i.e., separated subsets of the network with no interferograms spanning them) due to decorrelation associated with factors such as vegetation, cultivation, or snow cover, and especially after the network refinement Step 1-2. Additionally, some frames may have large acquisition gaps (several months or longer). It is noteworthy that even if the refined network of interferograms is fully connected, on an image-by-image basis, network gaps may still exist on a pixel-by-pixel basis. This is because each interferogram has a different coverage of valid unwrapped data due to the coherence-based masking applied to the LiCSAR products (see Section 2.1). In such cases, the design matrix $\mathbf{G}$ is rank deficient; Equation (2) can nevertheless be solved using singular value decomposition (SVD). However, the minimum-norm solution provided by SVD gives incremental displacements of zero in any network gaps, which is not realistic even for very small gaps (e.g., 6 days) where the true displacement would be almost zero, because noise in the interferograms between the gaps would not be close to zero.

To obtain the more realistic time series of the displacement even with a disconnected network, we follow the NSBAS method [19,50,53] that imposes a temporal constraint,

$$
\begin{bmatrix} \mathbf{d} \\ \mathbf{0} \end{bmatrix} =
\begin{bmatrix}
\begin{bmatrix} & \mathbf{G} & & \mathbf{0} & \mathbf{0} \end{bmatrix} \\
\gamma \begin{bmatrix}
1 & 0 & \dots & \dots & 0 & -t_1 & -1 \\
\vdots & \ddots & \ddots & & \vdots & -t_2 & \vdots \\
1 & \dots & 1 & \ddots & \vdots & \vdots & \vdots \\
\vdots & & \vdots & \ddots & 0 & \vdots & \vdots \\
1 & \dots & 1 & \dots & 1 & -t_{N-1} & -1
\end{bmatrix}
\end{bmatrix}
\begin{bmatrix} \mathbf{m} \\ v \\ c \end{bmatrix}
\tag{3}
$$

where γ is a scaling (weighting) factor of the temporal constraint, and we assume displacements are linear ($d = vt + c$). Solutions within the connected parts of the network are minimally affected by the temporal constraint provided γ is small (e.g., 0.0001). Thus, the temporal constraint part has an impact only on the connection across gaps in the network. Therefore, Equation (3) can be used for pixels with fully connected networks, as well as those with gaps.

If the actual displacements significantly deviate from a linear function (e.g., a coseismic jump due to an earthquake or acceleration/deceleration in displacement due to volcanic deformation), the solution between the gaps would become highly unreliable. In that case, functions other than linear, which we assume here (e.g., Heaviside, exponential, sinusoidal, etc.), might be better, but a priori information regarding the style of deformation is required to choose the appropriate function. Other functions are not currently implemented. Regardless, we can never retrieve a solution supported by the real observed data between the gaps. We should carefully consider the gaps when we interpret the time series of the displacement. LiCSBAS identifies and records the gaps for all pixels and increments, and this information can be easily displayed in the time series viewer to aid in the interpretation (see Section 2.5).

2.4.4. Step 1-4: Estimate Standard Deviation of the Velocity by Bootstrap

This step estimates the STD of the velocity from the cumulative displacements derived in Step 1-3 using the percentile bootstrap method [22,54]. The bootstrap approach creates a randomly resampled dataset with data replacement. We repeat the bootstrap resampling 100 times, compute the velocities during each iteration, and then calculate the STD for the ensemble of velocity solutions. High STD estimates indicate a noisy or nonlinear displacement time series. Note that the STD could be underestimated if the network is not fully connected, due to the temporal constraint in the SB inversion (Section 2.4.3).

2.4.5. Step 1-5: Mask Noisy Pixels in the Time Series

Time series can be obtained for all pixels with a sufficient number of available unwrapped data. However, the quality of a stack of unwrapped data may differ significantly from pixel to pixel. Some pixels may be very unreliable due to factors including remaining gaps and unwrapping errors.

To address this problem, Step 1-5 generates a mask for the time series to differentiate between "good" and "bad" pixels using several noise indices derived during the previous steps (Figure 3 and Table 1). The pixel is masked if any of the values of the noise indices for a pixel is worse (larger or smaller) than a specified threshold. The threshold for each noise index can be manually adjusted to obtain a better (i.e., harsher or gentler) mask for the time series and velocity.
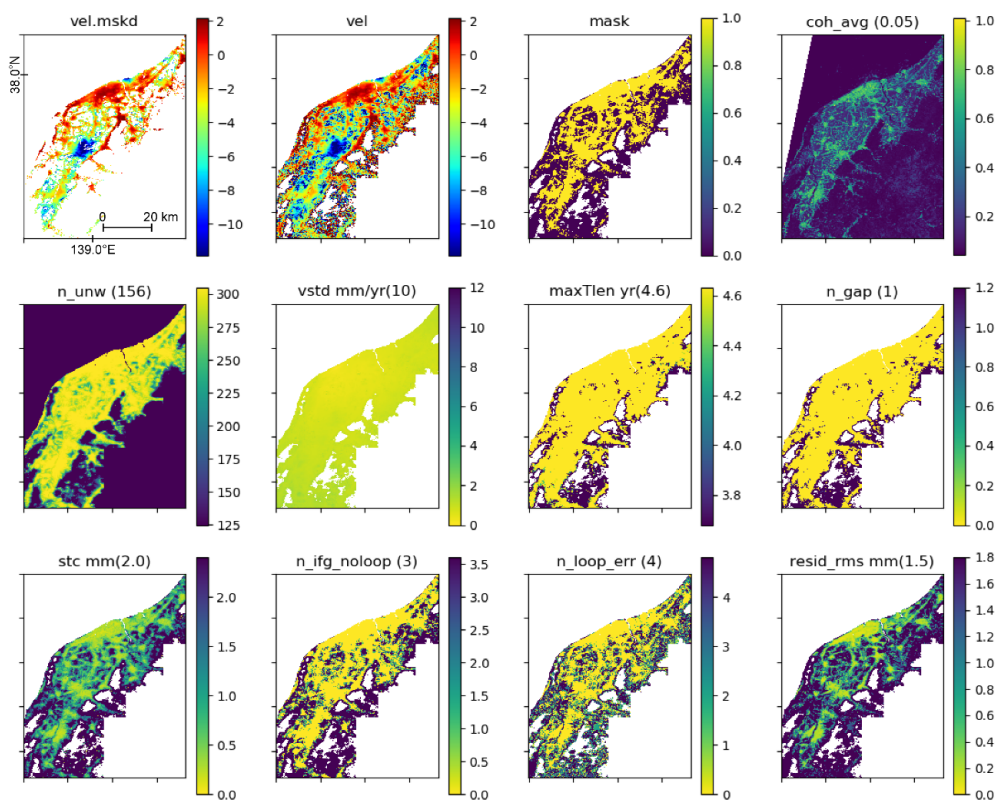
Figure 3. Example of the masking of velocities in noisy pixels derived from the time series analysis based upon a suite of indices for the region of the Echigo Plain (Section 4). Masked and unmasked velocities and the mask itself are shown along the top row (along with the average coherence from the input interferometric data), and the other images denote further noise indices used to create the mask (explanations and units given in Table 1). Numbers shown in the parentheses next to the titles of each noise index are the applied threshold value.

Table 1. List of the noise indices used for masking.

Noise index	Meaning
coh_avg	Average value of the interferometric coherence across the stack (0–1).
n_unw	Number of unwrapped data used in the time series calculation.
vstd	Standard deviation of the velocity (mm/yr) estimated in Step 1-4.
maxTlen	Maximum time length of the connected network (years). The larger the value, the better the precision network velocity estimate (see Section 3.5).
n_gap	Number of gaps in the interferogram network and time series breaks.
stc	Spatiotemporal consistency (mm) [55], which is the minimum root mean square (RMS) of the double differences of the time series in space and time between the pixel of interest and an adjacent pixel among all adjacent pixels.
n_ifg_noloop	Number of interferograms with no loops that cannot be checked by the loop closure and possibly have unidentified unwrapping errors.
n_loop_err	Number of the unclosed loops after the network refinement in Step 1-2.
resid_rms	RMS of residuals in the small baseline (SB) inversion (mm).

2.4.6. Step 1-6: Spatiotemporal Filtering of Time Series

The derived time series still includes some noise terms, including residual tropospheric noise, ionospheric noise, and orbital errors, which are, in general, spatially correlated and temporally uncorrelated. A spatiotemporal filter (i.e., high-pass in time and low-pass in space) can be applied to attempt to separate these noise components from the displacement time series [3,6]. To achieve

this filtering, we apply a one- and two-dimensional Gaussian kernel in time and space, respectively. Moreover, if the spatial scale of the target deformation signal is sufficiently small compared to the processing area (e.g., subsidence, landslides, or volcanic deformation), removing a ramp (linear, bilinear, or quadratic) from the entire area may help mitigate the noise.

It is noteworthy that too-strong a spatiotemporal filter (i.e., with long and short filter widths in time and space, respectively) can remove not only the noise components but also the actual displacement signals of interest, especially for cases where the displacement time series is nonlinear and the temporal width of the filter is too long compared to the time scale of the nonlinear displacement [6]. On the other hand, the temporal filter width needs to be sufficiently long, compared to the sampling interval, or no effect is produced. These issues have made separating noise from nonlinear displacements using infrequent data provided by earlier InSAR satellites (e.g., Envisat and ERS) challenging. However, with Sentinel-1, we can apply a relatively short temporal filter width and potentially more easily detect real nonlinear displacement. In LiCSBAS Step 1-6, we use $3\overline{dt}$ as the default temporal filter width (1σ of Gaussian), where $\overline{dt}$ is the average temporal sampling interval. For example, if the average temporal baseline of interferograms is 12 days, a temporal filter width of 36 days is applied to the displacement time series, which is sufficiently short to highlight seasonal displacements associated with the hydrological cycle [56,57].

2.5. Visualization of the Results

Interpretation of the derived time series is as important as the accurate derivation of the time series. However, the huge amount of associated data (e.g., ~4 GB for 100 images of an entire frame) often makes smooth visualization and intuitive interpretation problematic. Selection of an appropriate reference area is also a critical step towards obtaining meaningful and accurate displacements for interpretation, as all measurements are relative rather than in an absolute reference frame [23]. However, it is not possible to interactively examine and find out the appropriate reference by trial and error in most software.

LiCSBAS is equipped with an interactive time series viewer composed of two windows (graphical user interfaces). The first image window displays velocity, cumulative displacements, and noise indices (Figure 4a). When clicking on a pixel of interest, the associated time series with and without the spatiotemporal filter is promptly plotted in the second time series window (Figure 4b). Any network gaps are clearly displayed, which alerts the user to carefully interpret the time series connected by the temporal constraint (see Section 2.4.3). The reference area is shown by a black rectangle, and it can be interactively changed and examined in the image window.

The viewer can smoothly display the results of the time series analysis, even with a huge file size, without consuming a large amount of computer memory, owing to the HDF5 file format, from which the requested part of a large dataset can be quickly read.

(**a**)   (**b**)
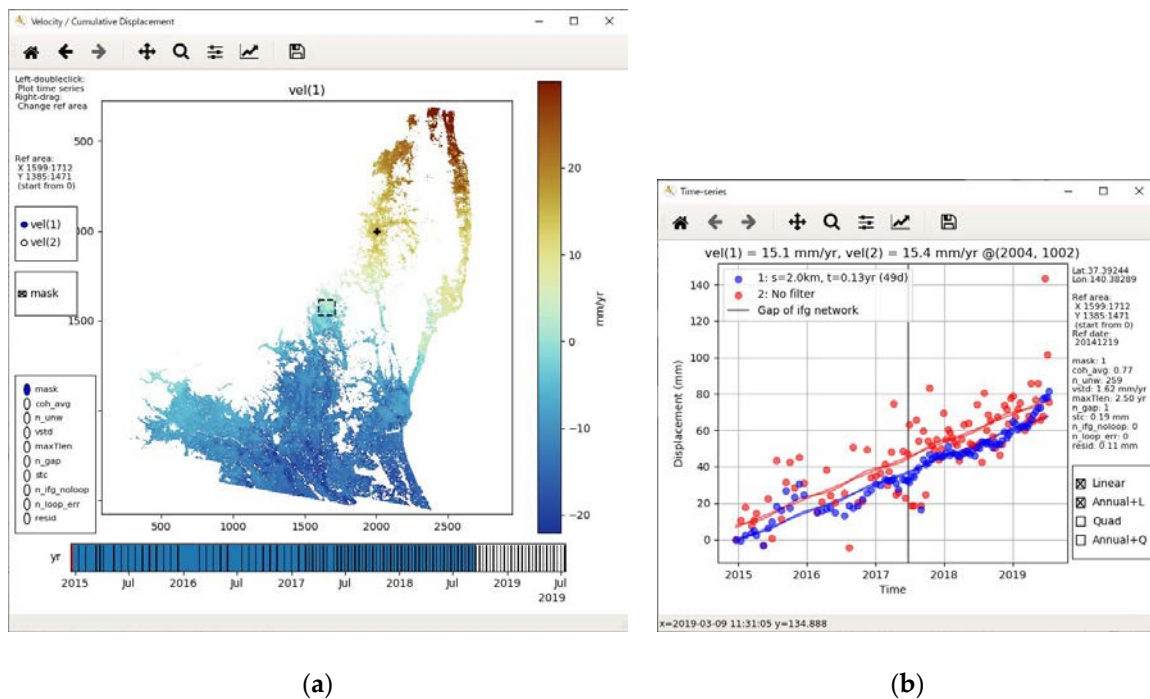
Figure 4. Example of the interactive time series viewer used to interpret the cumulative displacements, both spatially and through time, for the LiCSAR frame ID 046D_05292_131313 (Section 3). (**a**) Image window for the velocities, cumulative displacements, and noise indices (displayed in a nongeographic spatial reference given in pixels). A black dashed rectangle denotes the reference area, which can be changed by mouse operations. A black dot denotes the selected point of which the displacement time series is displayed in the time series window. Cumulative displacements at each acquisition epoch can be displayed by sliding the lower time panel. (**b**) Time series window for a selected point in the map denoted by a black dot. The red cumulative displacement points and model lines (with a linear or linear plus annual term shown here and a quadratic or quadratic plus annual term also available) indicate the unfiltered data, whilst those shown in blue have a spatial filter of 2 km and a temporal filter of 49 days applied, in this case. The model lines are calculated by post-fitting to the displacement time series and irrelevant to the temporal constraint function used in Step 1-3. A vertical black line denotes the gap in the interferogram network.

3. Case Study: Entire Frame

3.1. Southern Tohoku, Japan

We processed an entire LiCSAR frame covering Southern Tohoku and Northern Kanto, Japan in a descending orbit (LiCSAR frame ID 046D_05292_131313; acquisition time of day 20:42 UTC and 05:42 JST, Figure 5a). The observation period is from 25 November 2014 to 14 July 2019 (~4.6 years), and the associated network consists of 104 images and 306 interferograms. The acquisition interval is primarily 24 days prior to 18 February 2017 and 12 days after this date due to the increased observational capacity from the availability of Sentinel-1B, although all the data were acquired by Sentinel-1A (Figure 5b).

Inland areas within this frame are mostly mountainous and covered with dense vegetation. Furthermore, it snows during winter months. Therefore, it is quite difficult to obtain the full time series using C-band SAR data due to severe decorrelation. There are several plains and urban areas that are suitable for C-band data: the Kanto Plain in the south and the Echigo Plain in the northwest (Figure 5a).

A portion of the megathrust fault that slipped during the 2011 M_w 9.0 Tohoku earthquake is located offshore, just beyond the frame (Figure 5a) [58], although the frame encompasses a region that experienced a few meters of the eastward coseismic motion based on continuous Global

Step 1-2, we masked the northwestern portion of the frame including the Echigo Plain and the adjacent mountainous regions in Step 0-4 (Figure S2; its impact is discussed in Section 3.3). As a result, no interferograms were removed at Step 1-1, and only two interferograms (20141125–20141219 and 20160224–20160506) were removed at Step 1-2; there were no gaps in the network. We also applied the GACOS correction at Step 0-3 (its impact is discussed in Section 3.4). The filter widths used in Step 1-6 are 2 km in space and 49 days ($3\overline{dt}$) in time.
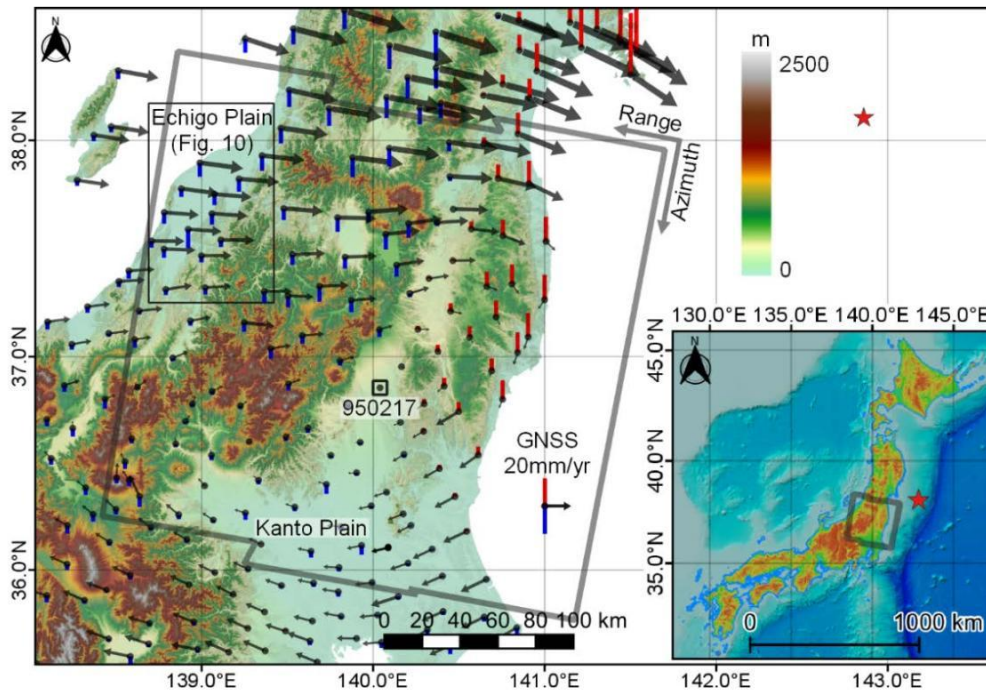
(**a**)
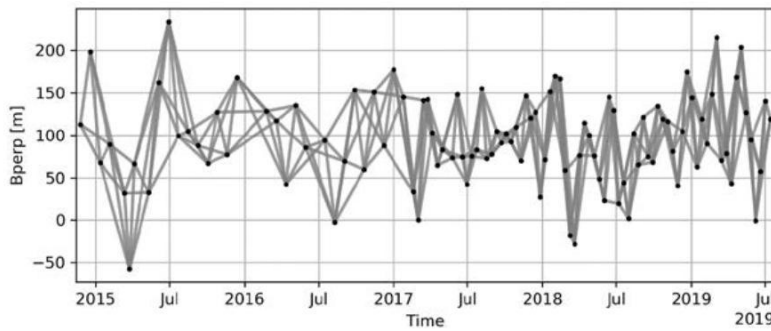
(**b**)

Figure 5. (**a**) Topography of the target area: Southern Tohoku and Northern Kanto, Japan. A black polygon denotes the area of the frame ID 046D_05292_131313. Black dots, black arrows, and red and blue bars denote Global Navigation Satellite System (GNSS) stations and associated horizontal and vertical velocities from 25 November 2014 to 14 July 2019. A small black square denotes the 950217 GNSS station, which is used as the reference point for the both GNSS- and synthetic aperture radar interferometry (InSAR)-derived surface displacements. (Inset) Location of the area of interest on Honshu in Japan. A black polygon and red star indicate the frame ID 046D_05292_131313 and the epicenter of the 2011 M_w 9.0 Tohoku Earthquake, respectively. (**b**) Perpendicular baseline configuration and network of the 306 SB interferograms formed from 104 Sentinel-1A images used in this study.

A portion of the megathrust fault that slipped during the 2011 M_w 9.0 Tohoku earthquake is located offshore, just beyond the frame (Figure 5a) [58], although the frame encompasses a region that experienced a few meters of the eastward coseismic motion based on continuous Global Navigation Satellite System (GNSS) observations [58]. The region has also experienced significant, ongoing postseismic deformation [59]. The rate of postseismic deformation has roughly converged to a constant velocity since around 2014 [60]. GNSS-derived velocities across the northern portion of the frame reveal significant eastward displacements at a rate of ~50 mm/yr from 2014–2019, compared to the south (Figure 5a). Vertical displacements are generally smaller than horizontal, but an east-to-west

transition from uplift to subsidence with rates on the order of >10 mm/yr occurs across the region covered by the northern portion of the frame.

As the inland mountainous regions tend to be decorrelated by vegetation and snow, the Echigo Plain is often isolated from the Kanto Plain in the unwrapped interferograms, which results in many unwrapping errors. To reduce the impact of these errors and improve the network refinement during Step 1-2, we masked the northwestern portion of the frame including the Echigo Plain and the adjacent mountainous regions in Step 0-4 (Figure S2; its impact is discussed in Section 3.3). As a result, no interferograms were removed at Step 1-1, and only two interferograms (20141125–20141219 and 20160224–20160506) were removed at Step 1-2; there were no gaps in the network. We also applied the GACOS correction at Step 0-3 (its impact is discussed in Section 3.4). The filter widths used in Step 1-6 are 2 km in space and 49 days ($3\overline{dt}$) in time.

3.2. Results

Despite having masked almost all pixels in the mountainous areas at Step 1-5 due to decorrelation, more than a million valid pixels, mainly distributed on the Kanto Plain and along northern basins and plains, still remain (Figure 6a). As a measure of InSAR data quality, we compare the LOS velocities with those stemming from the GNSS measurements with the same reference point of the 950217 GNSS station. The InSAR-derived velocities successfully image the broad tectonic deformation (i.e., LOS decrease in the northeast due to the combination of eastward and vertical uplift motions) and are largely consistent with the GNSS velocities (Figure 6a). The average and STD of the difference between InSAR and GNSS (n = 56) is 0.1 mm/yr and 1.9 mm/yr, respectively. We detect no significant systematic errors caused by factors such as ionospheric noise and orbital errors, despite no ionospheric correction having being applied in the LiCSAR products (Figure 6a,b). We also tried estimating the best-fitting quadratic polynomial surface through the differences between InSAR and GNSS velocities, at all GNSS stations, and subtracting it from the InSAR-derived velocities, which slightly decreased the STD to 1.6 mm/yr (Figure 6b). In this case, the impact of ionospheric noise and orbital errors is quite small, although, in some cases, these error sources could become significant, particularly at low latitudes on ascending tracks [61].

We also compare the LOS time series data and find that the InSAR-derived results are quite consistent with the GNSS measurements, even at the farthest GNSS site (950179) located 150 km away from the reference (950217; Figure 6c, Figure S5 and S6). The STD of the difference of the time series at each GNSS station shows no clear correlation with distance from the reference point (Figure 6d) once the GACOS correction has been applied, and the average of the STD of the difference at all GNSS stations is 9.0 mm, which represents the root-sum-square of the uncertainties of the InSAR- and GNSS-derived time series for each epoch. We also calculated the STD of the GNSS measurements for each epoch from the differences from those of 30-days moving average, and the average of the STD among all GNSS stations is 5.0 mm. Considering these, the uncertainty of the InSAR-derived time series for each epoch is 7.5 mm.

The results for Southern Tohoku demonstrate the potential of LiCSAR products and LiCSBAS to detect broad tectonic deformation independently without the help of GNSS and to contribute to dense and detailed tectonic strain mapping and global earthquake hazard assessment [62].

(a)   (b)

(c)   (d)
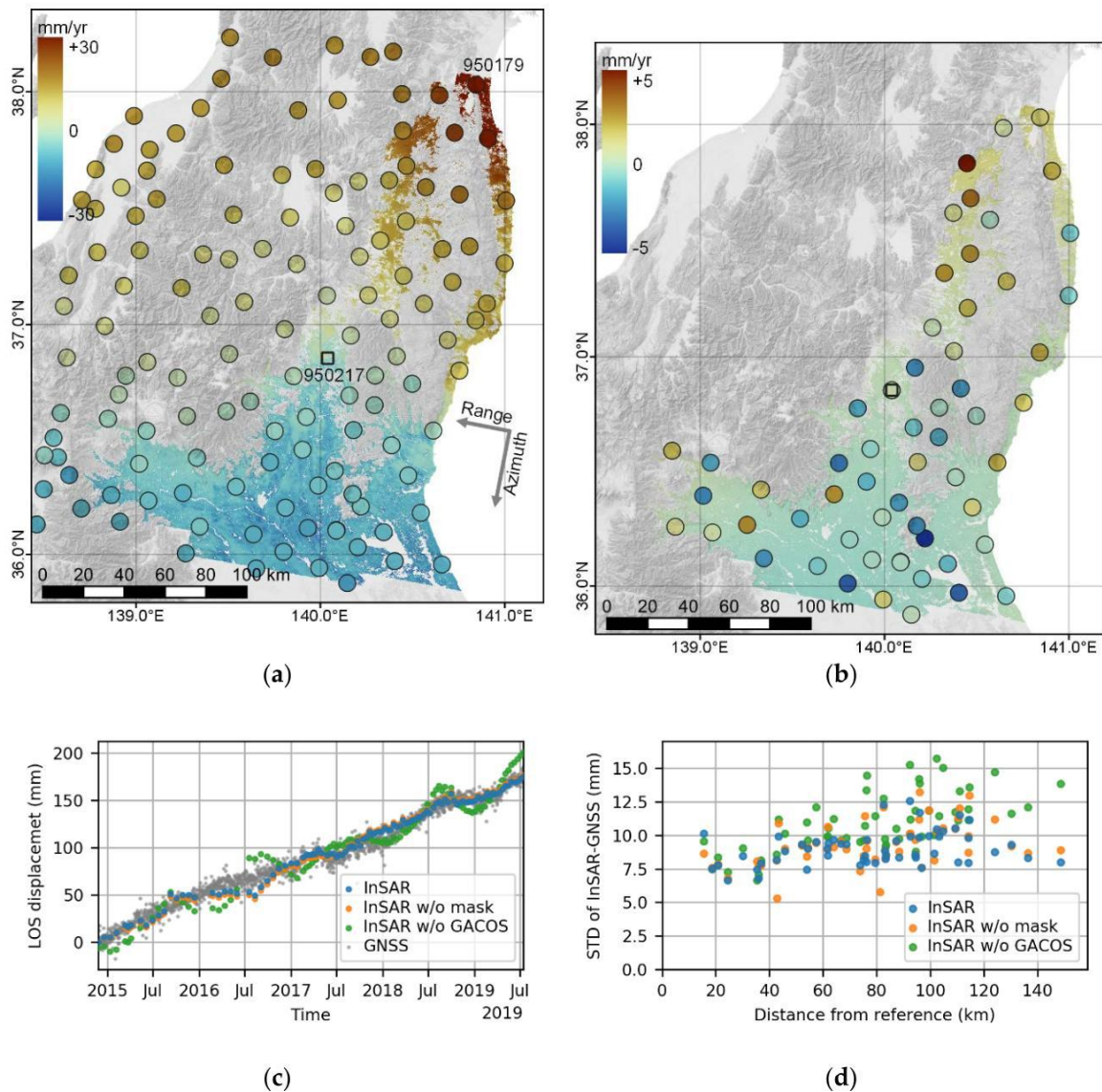
Figure 6. (a) Line-of-sight (LOS) velocity of InSAR (background colors) and GNSS (circles). Positive values mean displacement toward the satellite (i.e., uplift and/or eastward displacement, in this case). A black square denotes the reference GNSS point (950217). (b) Difference of the LOS velocity between InSAR and GNSS (colors in circles) and the estimated best-fit quadratic polynomial ramp. Note that the color scale is different from Figure 6a. (c) Displacement time series at 950179 (150 km away from the reference). The same ones for all the GNSS stations, and after removing the constant velocity (35.1 mm/yr) at 950179, are shown in Figures S5 and S6, respectively. (d) STD of the difference of the time series between InSAR and GNSS as a function of the distance from the reference point.

3.3. Impact of Masking and a Network Gap

Here, we investigate the impact of masking during Step 0-4. Without masking the northwestern area at Step 0-4, many unwrapping errors remain in the interferograms, and 47 interferograms are excluded during the loop closure at Step 1-2, generating a gap in the network between 18 and 30 June, 2017 (Figure S7). This means the masking has improved the network refinement and avoided the gap at the cost of a much-reduced extent of spatial coverage.

We compare the time series and velocities derived from the network, with and without the gap (i.e., with and without masking at Step 0-4). The time series at 950179 with the gap is consistent with the no-gap time series and the GNSS data, but slightly (~2 mm) biased across the gap (Figure 6c and Figure S6). This bias is caused by the interpolation associated with SB inversion linear temporal

The overall velocity, with and without the network gap, is also broadly similar, although significant differences up to ~5 mm/yr exist in some areas (Figure S8). The STD of the difference of the LOS velocity between InSAR with the gap and GNSS is 2.9 mm/yr, which is significantly larger than that without the gap (1.9 mm/yr). This is because the time length of the connected network, which has an impact on the precision of the velocity, is shortened from 4.6 years to 2.6 years by the gap (see Section 3.5).

3.4. Impact of the GACOS Correction

We investigate the impact of the GACOS correction at Step 0-3. In terms of SB interferograms, the STD of unwrapped phases for each entire interferogram is generally reduced (from 6.7 rad to 4.2 rad on average, from 6.0 rad to 3.9 rad on median), which indicates the GACOS correction significantly mitigated the tropospheric noise (Figure 7 and Figure S1).
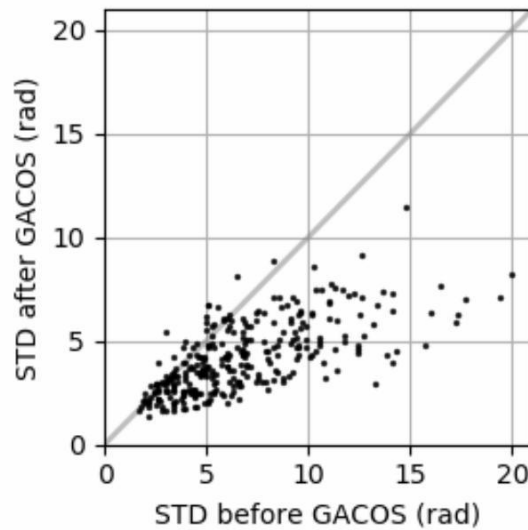
Figure 7. Correlation diagram of the STD of unwrapped phases in the 306 interferograms before and after the GACOS correction. The grey line denotes 1:1. The STD decreased from 6.7 rad to 4.2 rad on average and from 6.0 rad to 3.9 rad on median by the GACOS correction.

Regarding the result of the LiCSBAS processing, without the GACOS correction, the overall velocity is quite similar, and the STD of the difference in LOS velocity between InSAR and GNSS is 2.4 mm/yr, which is slightly larger than that with the GACOS correction (1.9 mm/yr; Figure 8).

The time series without GACOS at the distal position 950179 shows clear false seasonal displacements, presumably due to tropospheric noise, which has a seasonal correlation and cannot be removed by the spatiotemporal filter at Step 1-6 (Figure 6c, Figure S5, and Figure S6). The impact of the residual tropospheric noise depends on the distance from the reference point; far points tend to have larger time series STDs (Figure 6d). These results suggest that the GACOS correction plays an important role in more accurately retrieving the time series, especially at distances far from the reference point.

(**a**)   (**b**)
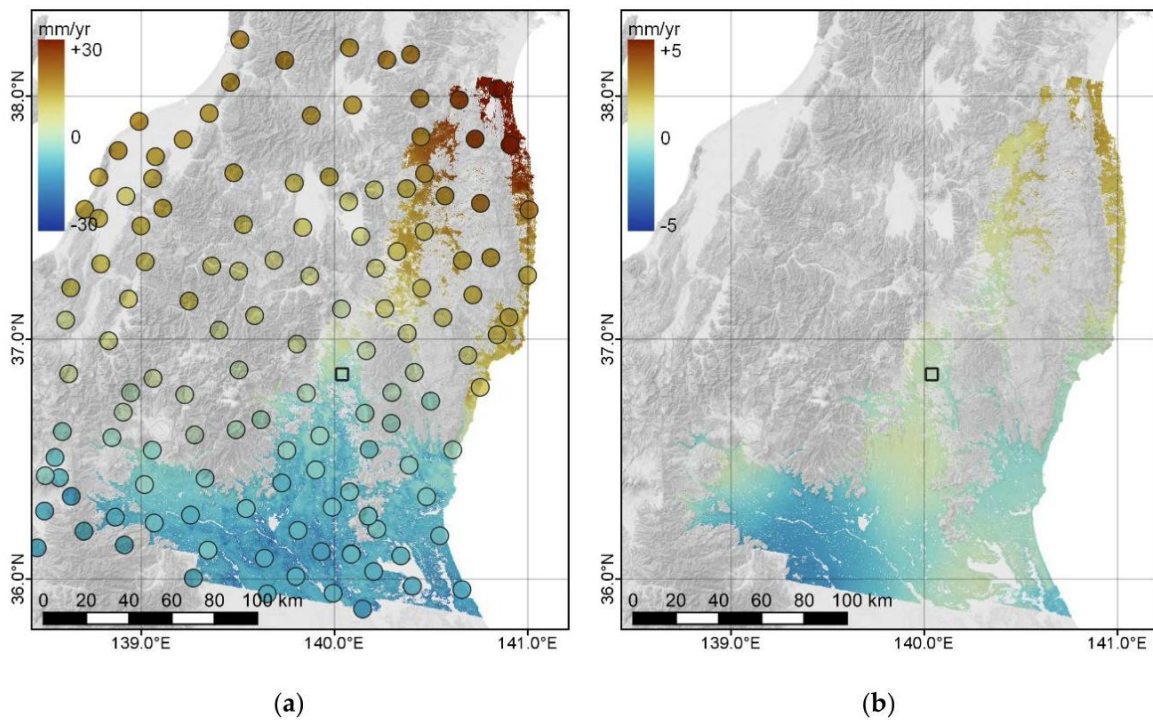
Figure 8: (**a**) LOS velocity without the GACOS correction. Symbols are the same as Figure 6a. (**b**) Difference of the LOS velocity with and without the GACOS correction (i.e., Figure 6a–Figure 8a). Note that the color scale is different from Figure 6a and Figure 8a.
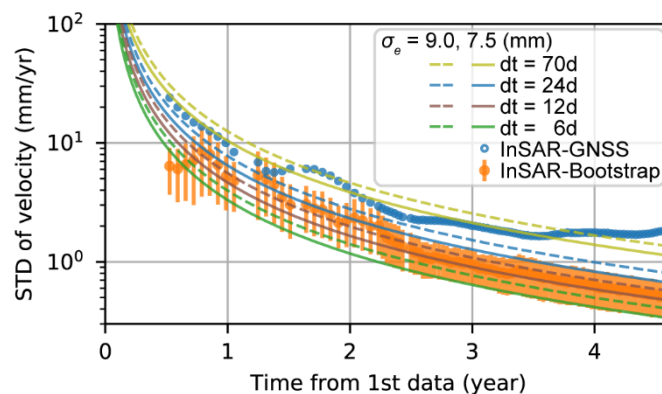
3.5. Evolution of Velocity Uncertainty

The velocity uncertainty σ_v can be estimated by

$$\sigma_v = \frac{2\sqrt{3}\sigma_e}{N^{0.5}T} \tag{4}$$

where σ_e, N, and T are the uncertainty at each epoch, the number of image data, and the observation time period length, respectively, under the assumption that the measurement errors are uncorrelated [63]. Note carefully that T is the network length. It is not equivalent to the time length of the observation period but, if there are no time gaps, T is equal to it. Therefore, the length of the gaps can significantly degrade the accuracy of the velocity estimation (see Section 3.3, the presence of a gap can significantly degrade the accuracy of the velocity estimation (see Section 3.3).

We calculate InSAR LOS velocities starting at the first Sentinel-1 acquisition (i.e., 25 November, 2014) to each subsequent acquisition using the present parameters, providing 25 periods, and the STD of each difference between the epoch GNSS LOS velocities calculated for the corresponding periods, and the STD of each difference between epoch using the present. We also compute the STD of the InSAR LOS velocity at each epoch using the parametric bootstrap method [22,54].

The temporal evolution of the InSAR-GNSS and InSAR bootstrap STDs are largely consistent with the theoretical velocity uncertainty of InSAR-GNSS and InSAR using Equation (4) with a range of 2.0 mm in the calculated inflection (i.e., by comparison with GNSS), respectively (4) and its sampling interval (i.e., calculated in Section 3.2 by comparison with GNSS, respectively. A sampling interval InSAR-GNSS STD) of 24 days to ~2.0 years (i.e., May–November 2017–2016), though the excursion by InSAR-GNSS is the amount time 2.0 years (Figure 9a, Figure No. S5 and S6). The STD of InSAR-GNSS converges to the ~2 mm/yr residuals (Figure 6a, Figure S5 and S6). The STD InSAR-GNSS noise component in InSAR and/or presumably because the discrepancies in the location of the measurement points in InSAR GNSS [63] or discrepancies in the locations of the measurement points between InSAR (i.e., coherent sum of the scatters in each resolution cell) and pointwise GNSS.

Our prediction of the velocity uncertainty is useful for estimating how small displacements can be detected given a certain amount of data or how long a time period is required to achieve a certain velocity precision. For example, if the sampling interval is 70 (corresponding to past Envisat

acquisitions every two cycles), 24, 12, or 6 (current best-case with Sentinel-1A/B) days, it would take 3.1, 2.2, 1.8, or 1.4 years to achieve a velocity STD of 2 mm/yr, respectively.


Figure 9. Temporal evolution of velocity uncertainties from the first acquisition (i.e., 25 November, 2014) to each subsequent acquisition with a log scale on the y-axis. Solid and dashed lines denote the theoretical values calculated from Eequation (4) with σ_e of 7.5 mm and 9.0 mm, respectively, and sampling intervals of 70, 24, 12, and 6 days. Blue dots denote the STD of the difference between InSAR and GNSS LOS velocities. Orange dots and error bars denote the average and STD of the InSAR LOS velocity STD computed by the bootstrap method.

Our prediction of the velocity uncertainty is useful for estimating how small displacements can be detected given a certain amount of data or how long a time period is required to achieve a certain velocity precision. For example, if the sampling interval is 70 (corresponding to past Envisat acquisitions every two cycles), 24, 12, or 6 (current best-case with Sentinel-1A/B) days, it would take 3.1, 2.2, 1.8, or 1.4 years to achieve a velocity STD of 2 mm/yr, respectively.

4. Case Study: Clipped Area

4.1. Echigo Plain

The Echigo (Niigata) Plain is located in the northwest of the frame ID 046D_05292_131313 (Figure 5a and Figure 10). It is an alluvial plain formed by the Shinano and Agano Rivers, surrounded by sea to the northwest and higher topography elsewhere (Figure 10). Snow cover is present in winter months in both the mountainous areas and the lowlands.

In addition to processing the whole frame (Section 3), we performed LiCSBAS processing after Step 0.3 (GACOS + clipping) using the Echigo Plain region 046D_05292_clipping. This area is a rectangular subset covering the Echigo Plain region by clipping this area from the entire frame (Step 0-5). In addition, we masked (Step 0-4) the mountainous areas to the southeast where most of the interferograms are decorrelated by precipitation and snow. Only one interferogram (20171203–20171227) was then excluded, due to unwrapping errors at Step 1-2, leaving 305 unwrapped interferograms for time series and velocity estimation. We selected GNSS station 960566 as a reference point, because the observed GNSS displacements are stable compared to other stations in this region and the associated InSAR-derived time series are reliable. As a result, clear displacement signals are detected at Niigata, Ojiya, and Sanjo cities (Figure 10b). In the following sections, we describe the details for each area as examples to test the extraction of both long-term subsidence signals and seasonally varying recoverable signals from the InSAR time series corroborated by independent datasets.
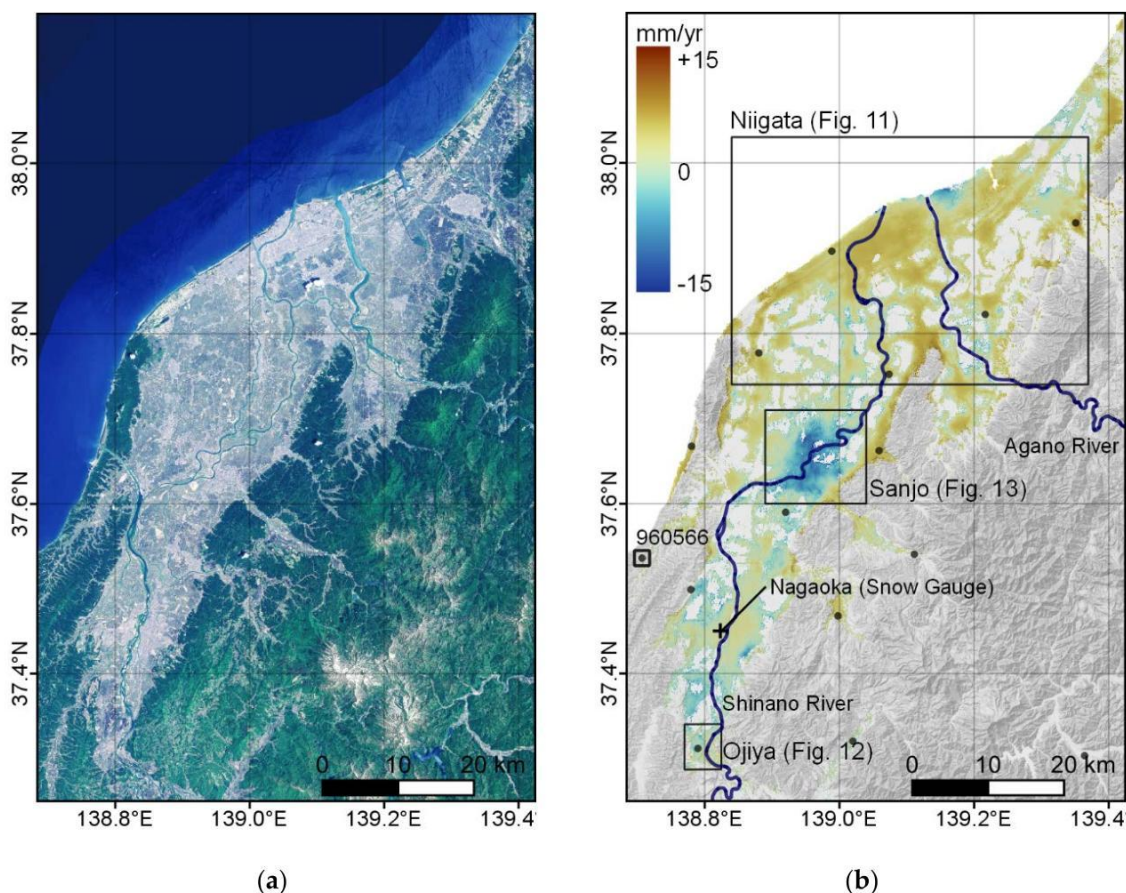
Figure 10. (**a**) Landsat 8 image of the Echigo Plain. (**b**) LOS velocity. Black dots denote GNSS stations. A black square denotes the reference point (960566).
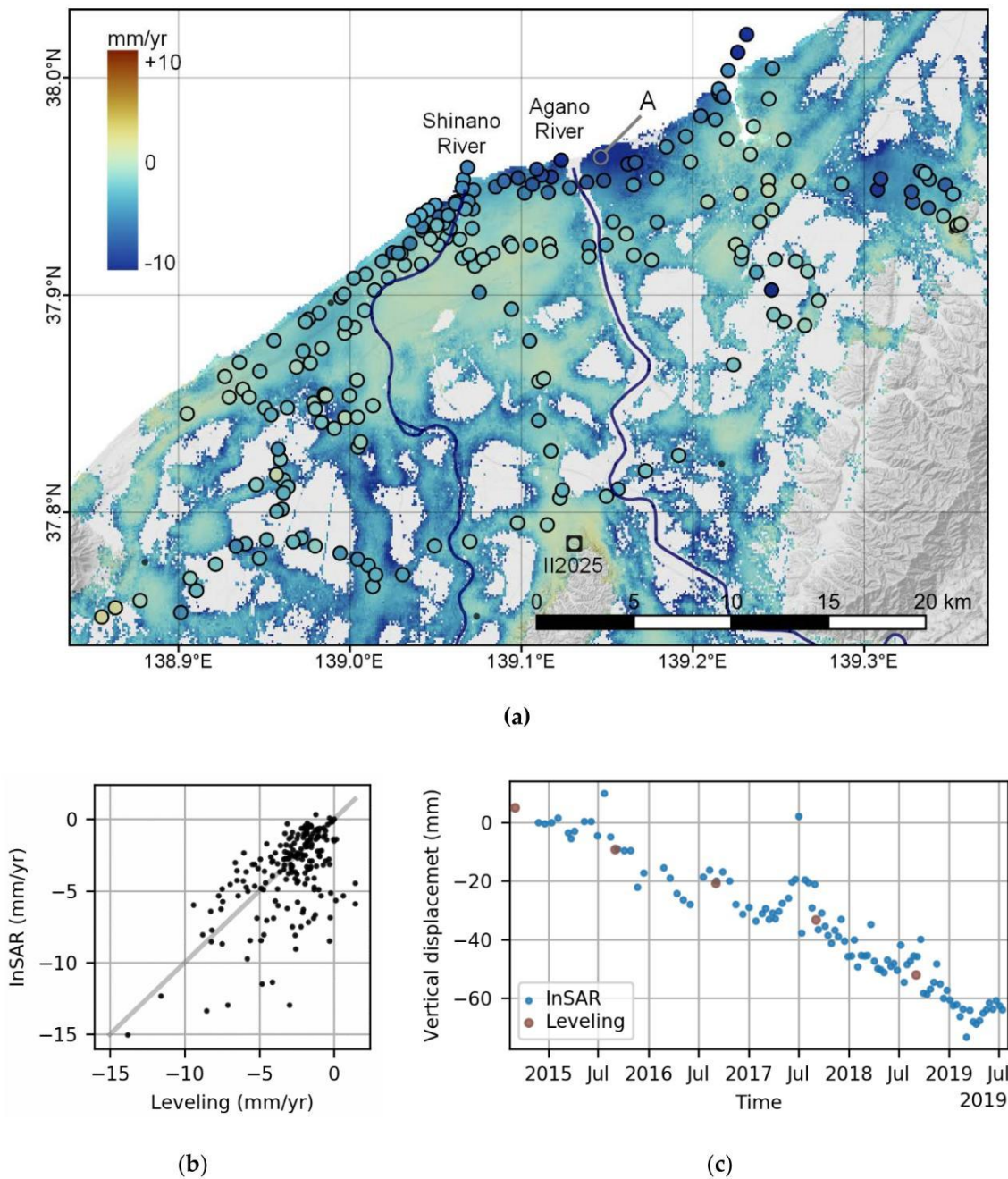
4.2. Niigata City

Niigata City was previously characterized by rapid subsidence (~50 cm/yr) associated with groundwater pumping and natural gas extraction around 1960 [64]. Since then, prevention measures have been taken to prevent subsidence, including regulation of extraction and restoration of groundwater. As a result, the subsidence rates have decreased, although slow subsidence (~2 cm/yr or less) is still detected around the mouth of the Agano River using conducted dense leveling surveys (Figure 11a) [65].

Here, we compare the vertical velocity between InSAR and leveling. We calculate the leveling-derived velocity at the benchmarks from five leveling surveys spanning September 2014 to September 2018. We project the InSAR-derived LOS velocity to vertical by taking into account the incidence angles under the assumption of no horizontal displacement. The reference point for both InSAR and leveling is set at benchmark II2025 (Figure 11a).

The derived vertical velocity shows an obvious correlation between InSAR and leveling with a degree of scattering (Figure 11b). The average and STD of the differences (n = 185) are 0.7 and 2.5 mm/yr, respectively. The time series of InSAR at benchmark A, where the most rapid subsidence has been observed, shows almost constant subsidence at a rate of 15.0 mm/yr, which is also consistent with leveling (13.8 mm/yr; Figure 11c). Note that the leveling results consist of only five data points and that the associated velocity uncertainty could be quite large compared to the GNSS and InSAR results. Therefore, the uncertainty of the InSAR-derived velocity estimate could be smaller than 2.5 mm/yr.

(a)

(b)

(c)

Figure 11. (a) Vertical velocities derived from InSAR (background colors) and leveling surveys (circles) in Niigata City. (b) Correlation diagram of the vertical velocity between InSAR and leveling. The grey line denotes a 1:1. (c) Time series of the vertical displacement at benchmark A just east of the mouth of the Agano River.

4.3. Ojiya City

Ojiya city is located on a terrace of the Shinano River (Figures 10 and 12). The Quaternary layer is composed of alluvium (thickness of 10–20 m), Holocene terrace deposits (5–20 m), lower terrace deposits (10–25 m), and Uonuma formation (> 450 m) from the top [66]. The deposits are mainly composed of gravel, sand, silt, and clay. The largest volumes of yearly groundwater usage in this area are devoted to snow-melting (38%) and industrial purposes (27%) [66]. The snow-melting system using the groundwater is laid along roads throughout the city (Figure 12a). The groundwater usage for snow-melting is concentrated in winter, which results in a sudden drop of the groundwater level every winter (Figure 12d and Figure S9).

for snow-melting is concentrated in winter, which results in a sudden drop of the groundwater level every winter (Figure 12d and Figure S9).

(**a**)

(**b**)

(**c**)

(**d**)
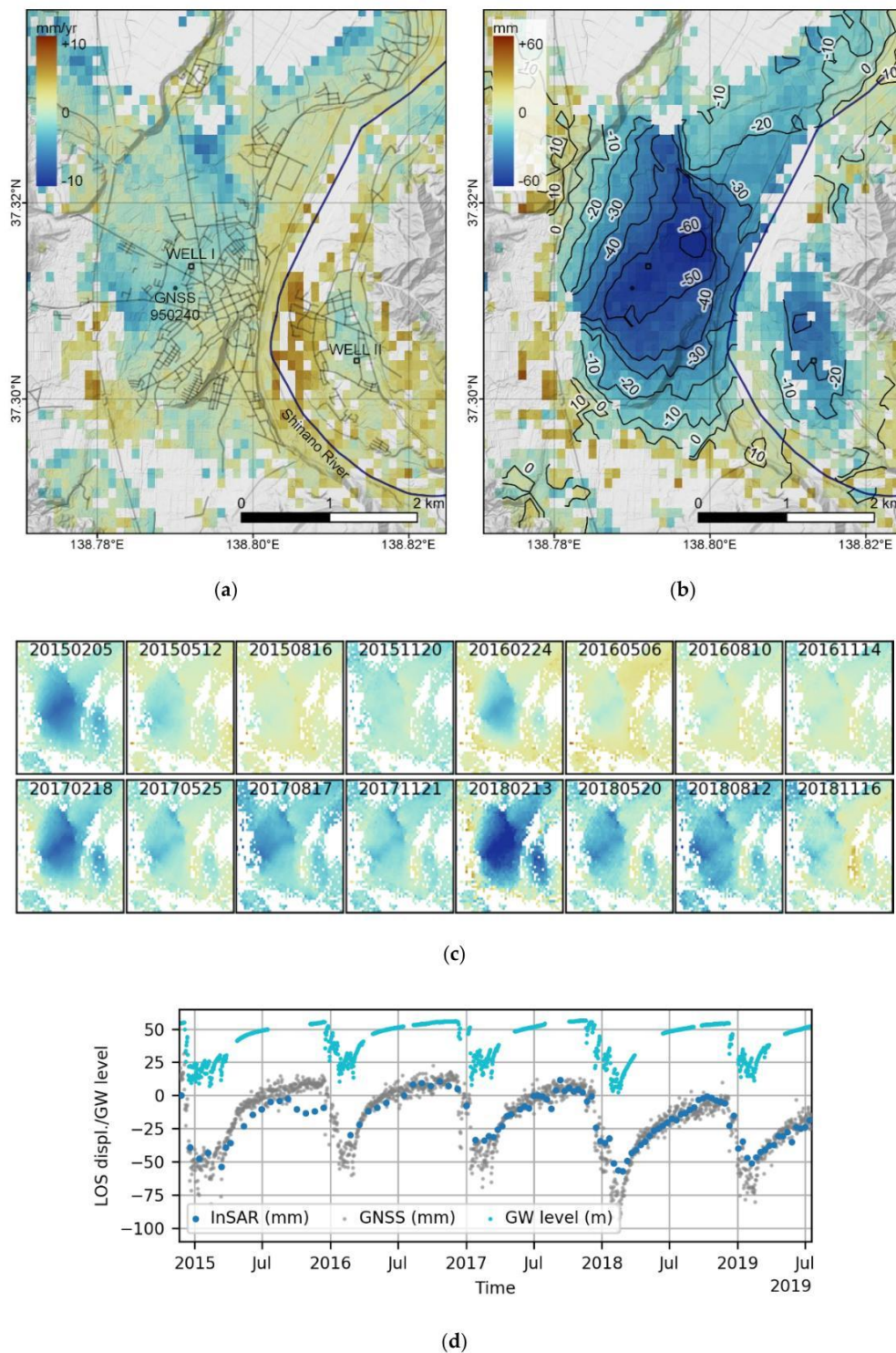
Figure 12. (**a**) Map of Ojiya City. Background color denotes the LOS velocity. Gray lines denote the distribution of the snow-melting system. (**b**) LOS displacement on 13 February 2018. (**c**) Cumulative LOS displacements with reference to the first acquisition of 25 November 2014. The acquisition dates (yyyymmdd) are shown on the top of each figure. The color range is the same as Figure 12b. All the acquisitions are shown in Figure S11. (**d**) Time series of the LOS displacement derived from InSAR and GNSS at 950240, and the groundwater level at Well I.

A continuous GNSS station (950240) has recorded large seasonal vertical displacements since 1996 (Figure 12d and Figure S9) with subsidence starting around December, when winter snowfall begins [67]. When the accumulated snow melts away around March, recovery of the subsidence begins, exponentially decays, and then converges in autumn. This temporal evolution of vertical displacements is consistent with the groundwater level in Well I, which is located 300 m northeast of the GNSS station (Figure 12d, Figures S9 and S10) [67]. The periodic subsidence is almost completely recovered every year, and interannual subsidence hardly remains. The depth of Well I is 200 m, and the screens are located at the depth of 134–189 m, corresponding to the Uonuma formation. These facts suggest the predominant mechanism of this vertical fluctuation is elastic compaction and expansion of the aquifer in the Uonuma formation, rather than inelastic [67,68].

Here, we reveal the spatial extent of the vertical fluctuations, as well as the detailed temporal evolution. We computed the InSAR-derived LOS time series and velocity with reference to the GNSS station 960566 (~26 km north-northeast from 950240). Although the velocity shows no significant long-term subsidence (Figure 12a), the time series clearly captures the periodic subsidence and retrieval temporally and spatially in detail (Figure 12c,d and Figure S11). The distribution of the fluctuating areas is almost the same every year.

The InSAR-derived time series at 950240 closely agrees with the time series measured by GNSS (Figure 12d). The STD of the difference between the two datasets is 9.5 mm, which is consistent with the result for the entire frame (Section 3.2), even with the large nonlinear periodic displacement. In February 2018, the subsidence was larger than the other years, presumably because the amount of snowfall was the largest that winter of 2018, and this is also clearly captured in the InSAR results (Figure 12c,d and Figure S11; see also Section 4.4).

In terms of the spatial distribution, there are two peaks of the subsidence either side of the river (Figure 12b,c). The eastern one has a smaller amount of the subsidence than the western one, which is consistent with the fact that the groundwater level change at the eastern Well II is smaller than that at the western Well I (Figure S9). The shape of the western subsidence bowl is not asymmetric; the northeast and southwest edges of the subsidence area have sharp boundaries that may be controlled by subsurface geological boundaries.

4.4. Sanjo City

Large subsidence rates measured in Sanjo City (Figures 10b and 13a) correspond to time series (Figure 13b) that do not exhibit linear displacements like Niigata City (Figure 11c) but, rather, are characterized by episodic subsidence (~4 cm) in the winter of 2017/2018, which is not recovered thereafter. This suggests a mechanism that is not elastic but inelastic. In addition to the episodic displacement, periodic displacements, as in Ojiya City (i.e., subsidence in winter and recovery until autumn), are also seen in the time series (Figure 13b). This is expected, because Sanjo City employs the same type of snow-melting system that we previously described. The height difference of the periodic component is ~3 cm, which is smaller than the Ojiya City signal (~6 cm or more).

One possible explanation for the episodic subsidence in the winter of 2017/2018 relates to overpumping of the groundwater for snow-melting. An unusually heavy snowfall occurred in this region on 30 January 2018, and the snow remained uncharacteristically deep (>100 cm) until the end of February, whilst the normal depth of snow is ~60 cm (Figure 13b), recorded at the Nagaoka snow gauge, ~25 km SSW from Sanjo City (Figure 10b). The episodic subsidence observed from 1 to 25 February is temporally consistent with the heavy snowfall.

(**a**)

(**b**)
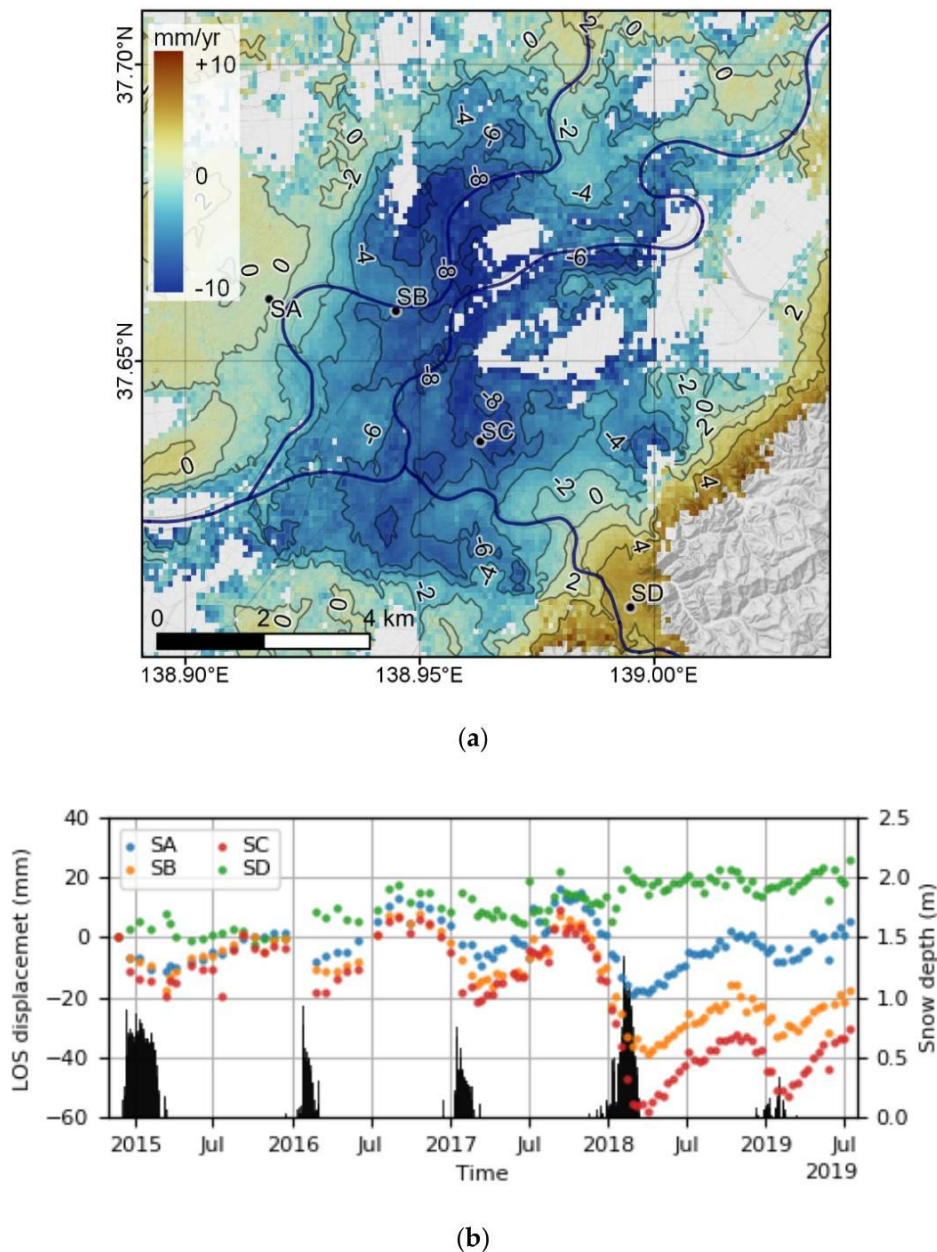
Figure 13. (**a**) LOS velocity in Sanjo City. (**b**) Time series of the LOS displacement at SA-SD of which
locations are shown in (a), and snow depth at the Nagaoka snow gauge (the location is shown in
Figure 10b).

4.5. Annual Displacement in Echigo Plain

Here, we briefly present the annual displacements over the Echigo Plain, which we estimate
from the time series using least-squares. Although the actual periodic displacement is not strictly
sinusoidal (Figures 12d and 13b), for simplicity, we use a simple sinusoidal function, along with the
linear function, to estimate the amplitude and time offset (e.g., [57,69]).

Large amplitudes are detected in Ojiya City (~22 mm) and Sanjo City (~13 mm), as was previously
shown in Sections 4.3 and 4.4 (Figure 14a). Some other areas also exhibit relatively large amplitudes,
including Nagaoka City (~17 mm) and Shibata City (~11 mm). Elsewhere, only moderate amplitude
signals ranging from 4–7 mm/yr are detected. The spatial pattern revealed by the amplitude map might
reflect variations in geological properties. We should note that if the reference point had a periodic
displacement, an apparent inverse periodic displacement would erroneously be generated for all the
other areas. However, it is unlikely, because some of the valley plains (e.g.,

southeast of Sanjo City), which should have different geological properties from the Echigo Plain, show very low amplitudes (< 2 mm).

The estimated time offset is almost constant over the Echigo Plain (Figure 14b). The lower peak of the annual displacements occurs around February and March, implying that periodic displacements occur simultaneously, and the common cause is groundwater pumping for snow-melting.
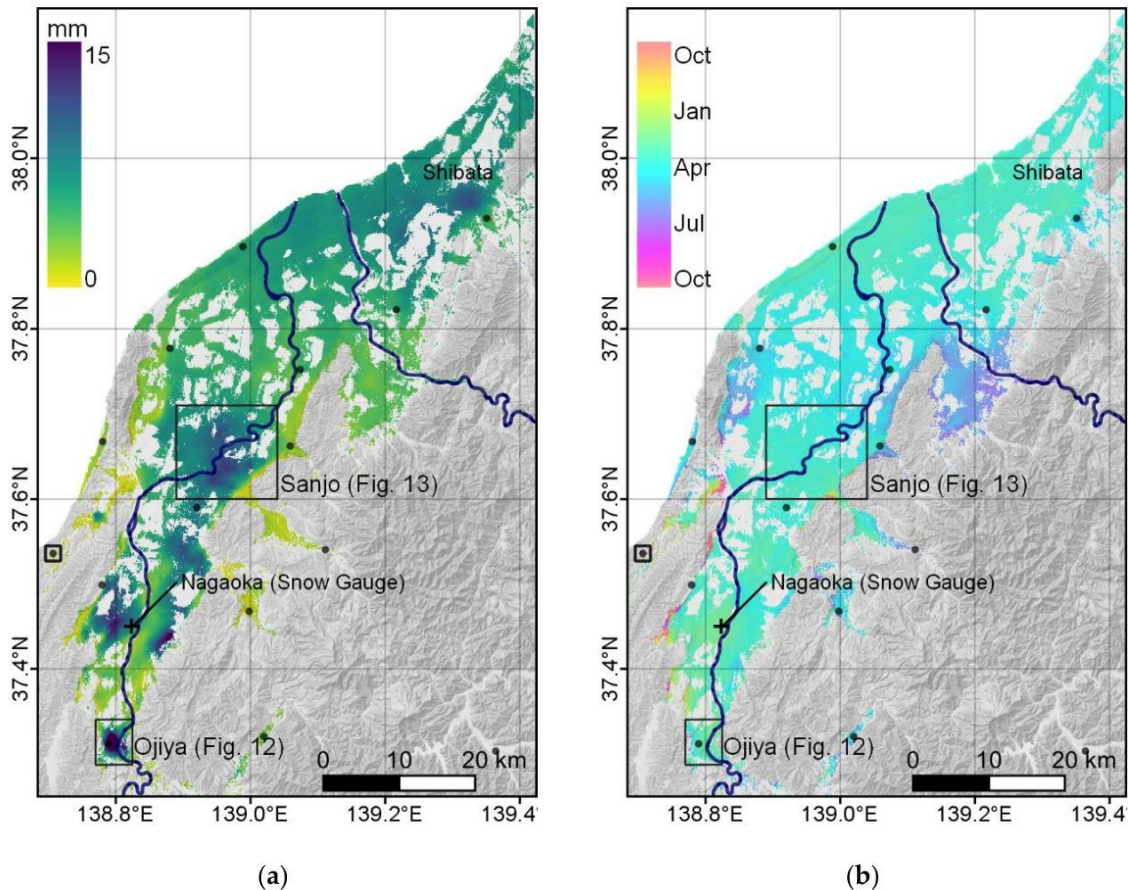

(a) (b)

Figure 14. (a) Amplitude of the annual displacement in the Echigo Plain. (b) Timing of the lower peak of the annual displacement.

The estimated time offset is almost constant over the Echigo Plain (Figure 14b). The lower peak of the annual displacements occurs around February and March, implying that periodic displacements occur simultaneously, and the common cause is groundwater pumping for snow-melting.

5. Discussion

5.1. Processing Time and Disk Usage

For most existing InSAR time series analysis software packages (e.g., StaMPS or GIAnT), users generally need to produce the interferograms over the area of interest themselves. If we start by downloading a stack of Sentinel-1 SLC data and then produce a whole set of the interferograms, the process takes a large amount of time and disk space. In our example, to produce 100 images and ~300 interferograms used in the case study, InSAR processing and SBC products must be downloaded, and ~600 GB data for time series analysis must be created, along with ~300 GB of interferograms and other intermediate files.

One of the advantages of LiCSBAS is that it uses the LiCSAR products, extensive knowledge of InSAR processing and Sentinel-1 data is also not needed to prepare the data. The size of GeoTIFF files for ~300 interferograms is only ~5 GB (Table 2). The size of the files produced by the LiCSBAS stage of LiCSBAS is small (~30 GB), and LiCSBAS processing programs are also reasonable, therefore LiCSBAS saves significant time and disk space. The size of GeoTIFF files for ~300 interferograms is only ~5 GB (Table 2). The size of the files

produced by LiCSBAS for the Japan test frame is only ~30 GB. LiCSBAS processing times are also reasonable, even for an entire frame (~5 hours; Table 2). The estimates presented here are based on an Intel Xeon E5-2690 CPU (8 cores, 2.90 GHz), ~5 GB maximum of used RAM, and a download speed of ~30 MB/sec. Further, if the area of interest is a specific part within the frame, clipping at Step 0-5 greatly saves processing time and disk space but also could improve the result because of reducing the impact of potential unwrapping errors (Section 4).

Table 2. Processing time and disk usage of LiCSBAS in the case studies.

	Entire Frame	Echigo Plain	Entire Frame (10 × 10 Downsampled)
Size of Image	3338 × 2685	732 × 922	333 × 268
# of Images	104	104	104
# of Interferograms	306	306	306
# of Inverted Pixels (at Step 1-3)	2,503,334	288,079	24,579
# of Remaining Pixels (after Step 1-6)	1,166,756	167,269	15,704
Step 0-1	10 min	—	—
Step 0-2	10 min	—	3 min
Step 0-3	30 min	—	5 min
Step 0-4	5 min	2 min	1 min
Step 0-5	—	5 min	—
Step 1-1	2 min	<1 min	<1 min
Step 1-2	20 min	4 min	3 min
Step 1-3	3 hr 30 min	25 min	5 min
Step 1-4	20 min	2 min	<1 min
Step 1-5	<1 min	<1 min	<1 min
Step 1-6	30 min	5 min	2 min
Total Time for Step 1	~5 hr	~40 min	~10 min
Size of Downloaded GeoTIFF	5 GB	—	—
Size of GACOS Data	5 GB	—	—
Size of Converted Data	21 GB	2 GB	0.2 GB
Size of Created Data in Step 1	10 GB	1 GB	0.2 GB

Downsampling at Step 0-2 makes further processing much faster and file sizes much smaller at the cost of resolution (Table 2), whilst broadly, the same result can be derived (Figure S12). If the full resolution (~100 m) is not required (e.g., for large-scale strain estimation), downsampling is worth incorporating. Even when full resolution is preferred as the final result, quick processing with the downsampled dataset is useful to check if a good result can be obtained and to adjust parameters/thresholds prior to processing at full or higher resolution.

5.2. Limitations

The interferograms provided by LiCSAR are multilooked to ~100 m resolution and strongly spatially filtered for the main purpose of the LiCS project (i.e., large-scale deformation monitoring and tectonic strain mapping), as mentioned in Section 2.1. Although km-scale deformations can be accurately detected, as demonstrated in Section 4, the LiCSAR products are not optimized for more localized deformation studies such as infrastructure monitoring.

LiCSBAS deals with gaps in the SB network by imposing a temporal constraint at the inversion step (Step 1-3; Section 2.4.3). We note that the interpolated displacement between the gaps might not be realistic if the true deformation is not linear. It is difficult to quantify the uncertainty of the derived

time series with gap, and the potential bias should be carefully considered. Gaps are easily identified in the time series viewer to aid in interpretation.

Densely vegetated areas, including large portions of Japan, suffer from incoherence in C-band data, even with the short temporal baselines of Sentinel-1, compared to earlier radar satellites (see Section 3). In this study, the minimum acquisition interval is 12 days versus 6 days for Sentinel-1 across Europe [12]. Quite a few of the 12-day interferograms retain sufficient coherence over the frame, whereas most of the 24-day and longer interferograms lose coherence in the vegetated areas (Figure S13). In general, the coherence decays exponentially with time [70,71]. More frequent acquisition intervals (i.e., 6 days) increase the likelihood of retaining coherence at C-band and detecting deformation over vegetated areas [72].

Another possible solution for the vegetated areas is exploitation of L-band data. Although abundant L-band data like Sentinel-1 are currently not available, several new planned L-band satellites missions, such as ALOS-4 and NISAR, are capable of frequent, wide-swath observations. LiCSBAS can also be used to process data from other satellites (see Section 2.2).

6. Conclusions

We have developed LiCSBAS as an open-source InSAR time series analysis package integrated with the automated LiCSAR processing chain outputs. LiCSBAS utilizes published LiCSAR products, and users do not need to produce interferograms from SLC data, thus avoiding high data processing time and disk space consumption. LiCSBAS automatically identifies and removes interferograms with many unwrapping errors by the loop closure test and estimates reliable time series and velocities with the help of masking based upon several noise indices. All processing steps are easy to run using a batch script, and users can adjust processing parameters to obtain improved results. The interactive time series viewer aids in the interpretation of the derived displacements.

Case studies presented here over Japan demonstrate that LiCSBAS can detect both large-scale and localized deformation with an accuracy of < 1 cm at each epoch and ~2 mm/yr in velocity. These results are validated by comparisons with GNSS and leveling data. Displacements with different temporal characteristics, such as linear, periodic, and episodic, in the Echigo Plain are also successfully and accurately detected.

LiCSBAS enables users to easily perform InSAR time series analysis without producing interferograms, thus facilitating the use of globally available and abundant Sentinel-1 data for a wide range of scientific investigations.

Conflicts of Interest: The authors declare no conflicts of interest.

References

1. Zhou, X.; Chang, N.-B.; Li, S. Applications of SAR Interferometry in Earth and Environmental Science Research. *Sensors* **2009**, *9*, 1876–1912. [CrossRef]

2. Elliott, J.R.; Walters, R.J.; Wright, T.J. The role of space-based observation in understanding and responding to active tectonics and earthquakes. *Nat. Commun.* **2016**, *7*, 13844. [CrossRef]

3. Hooper, A.J.; Bekaert, D.; Spaans, K.; Arikan, M. Recent advances in SAR interferometry time series analysis for measuring crustal deformation. *Tectonophysics* **2012**, *514–517*, 1–13. [CrossRef]

4. Osmanoğlu, B.; Sunar, F.; Wdowinski, S.; Cabral-Cano, E. Time series analysis of InSAR data: Methods and trends. *ISPRS J. Photogramm. Remote Sens.* **2016**, *115*, 90–102. [CrossRef]

5. Ferretti, A.; Prati, C.; Rocca, F. Permanent Scatters in SAR Interferometry. *IEEE Trans. Geosci. Remote Sens.* **2001**, *39*, 8–20. [CrossRef]

6. Hooper, A.; Segall, P.; Zebker, H. Persistent scatterer interferometric synthetic aperture radar for crustal deformation analysis, with application to Volcán Alcedo, Galápagos. *J. Geophys. Res. Solid Earth* **2007**, *112*, 1–21. [CrossRef]

7. Berardino, P.; Fornaro, G.; Lanari, R.; Sansosti, E. A new algorithm for surface deformation monitoring based on small baseline differential SAR interferograms. *IEEE Trans. Geosci. Remote Sens.* **2002**, *40*, 2375–2383. [CrossRef]

8. Ferretti, A.; Fumagalli, A.; Novali, F.; Prati, C.; Rocca, F.; Rucci, A. A new algorithm for processing interferometric data-stacks: SqueeSAR. *IEEE Trans. Geosci. Remote Sens.* **2011**, *49*, 3460–3470. [CrossRef]

9. Tong, X.; Sandwell, D.T.; Smith-Konter, B. High-resolution interseismic velocity data along the San Andreas Fault from GPS and InSAR. *J. Geophys. Res. Solid Earth* **2013**, *118*, 369–389. [CrossRef]

10. Hussain, E.; Wright, T.J.; Walters, R.J.; Bekaert, D.P.S.; Lloyd, R.; Hooper, A. Constant strain accumulation rate between major earthquakes on the North Anatolian Fault. *Nat. Commun.* **2018**, *9*, 1392. [CrossRef]

11. Homepage | Copernicus. Available online: https://www.copernicus.eu/en (accessed on 27 November 2019).

12. Potin, P.; Rosich, B.; Miranda, N.; Grimont, P.; Shurmer, I.; O'Connell, A.; Krassenburg, M.; Gratadour, J.-B. Copernicus Sentinel-1 Constellation Mission Operations Status. In *Proceedings of the IGARSS 2019—2019 IEEE International Geoscience and Remote Sensing Symposium*; IEEE: Yokohama, Japan, 2019; pp. 5385–5388. [CrossRef]

13. Sandwell, D.; Mellors, R.; Tong, X.; Wei, M.; Wessel, P. Open radar interferometry software for mapping surface Deformation. *Eos Trans. Am. Geophys. Union* **2011**, *92*, 234. [CrossRef]

14. gmtsar: GMTSAR. Available online: https://github.com/gmtsar/gmtsar (accessed on 27 November 2019).

15. Rosen, P.A.; Gurrola, E.; Sacco, G.F.; Zebker, H. The InSAR scientific computing environment. In Proceedings of the IEEE EUSAR 2012 9th European Conference on Synthetic Aperture Radar, Nuremberg, Germany, 23–26 April 2012.

16. isce2: InSAR Scientific Computing Environment Version 2. Available online: https://github.com/isce-framework/isce2 (accessed on 27 November 2019).

17. STEP | Science Toolbox Exploitation Platform. Available online: http://step.esa.int/main/ (accessed on 27 November 2019).

18. Agram, P.S.; Jolivet, R.; Riel, B.; Lin, Y.N.; Simons, M.; Hetland, E.; Doin, M.-P.; Lasserre, C. New Radar Interferometric Time Series Analysis Toolbox Released. *Eos Trans. Am. Geophys. Union* **2013**, *94*, 69–70. [CrossRef]

19. Agram, P.; Jolivet, R.; Simons, M. Generic InSAR Analysis Toolbox (GIAnT)—User Guide. Available online: http://earthdef.caltech.edu (accessed on 27 November 2019).

20. MintPy: Miami InSAR Time-Series Software in Python. Available online: https://github.com/insarlab/MintPy (accessed on 27 November 2019).

21. Yunjun, Z.; Fattahi, H.; Amelung, F. Small baseline InSAR time series analysis: Unwrapping error correction and noise reduction. *Comput. Geosci.* **2019**, *133*, 104331. [CrossRef]

22. StaMPS: Stanford Method for Persistent Scatterers. Available online: https://github.com/dbekaert/StaMPS (accessed on 27 November 2019).

23. Galve, J.; Pérez-Peña, J.; Azañón, J.; Closson, D.; Caló, F.; Reyes-Carmona, C.; Jabaloy, A.; Ruano, P.; Mateos, R.; Notti, D.; et al. Evaluation of the SBAS InSAR Service of the European Space Agency's Geohazard Exploitation Platform (GEP). *Remote Sens.* **2017**, *9*, 1291. [CrossRef]

24. Cignetti, M.; Manconi, A.; Manunta, M.; Giordan, D.; De Luca, C.; Allasia, P.; Ardizzone, F. Taking Advantage of the ESA G-POD Service to Study Ground Deformation Processes in High Mountain Areas: A Valle d'Aosta Case Study, Northern Italy. *Remote Sens.* **2016**, *8*, 852. [CrossRef]

25. ARIA Products. Available online: https://aria-products.jpl.nasa.gov/ (accessed on 27 November 2019).

26. Bekaert, D.; Karim, M.; Justin, L.; Hua, H.; Agram, P.; Owen, S.; Manipon, G.; Malarout, N.; Lucas, M.; Sacco, G.; et al. Development and Dissemination of Standardized Geodetic Products by the Advanced Rapid Imaging and Analysis (ARIA) Center for Natural Hazards. In Proceedings of the International Union of Geodesy and Geophysics (IUGG), Montreal, Canada, 8–18 July 2019.

27. ARIA-Tools: Tools for Exploiting ARIA Standard Products. Available online: https://github.com/aria-tools/ARIA-tools (accessed on 27 November 2019).

28. Wegmüller, U.; Werner, C.; Strozzi, T.; Wiesmann, A.; Frey, O.; Santoro, M. Sentinel-1 Support in the GAMMA Software. *Procedia Comput. Sci.* **2016**, *100*, 1305–1312. [CrossRef]

29. Werner, C.; Wegmüller, U.; Strozzi, T.; Wiesmann, A. GAMMA SAR and interferometric processing software. In Proceedings of the ERS-Envisat Symposium, Gothenburg, Sweden, 16–20 October 2000.

30. COMET-LiCS Sentinel-1 InSAR Portal. Available online: https://comet.nerc.ac.uk/COMET-LiCS-portal/ (accessed on 27 November 2019).

31. LiCSBAS: LiCSBAS Package to Conduct InSAR Time Series Analysis Using LiCSAR Products. Available online: https://github.com/yumorishita/LiCSBAS (accessed on 27 November 2019).

32. Scheiber, R.; Moreira, A. Coregistration of interferometric SAR images using spectral diversity. *IEEE Trans. Geosci. Remote Sens.* **2000**, *38*, 2179–2191. [CrossRef]

33. Prats-Iraola, P.; Scheiber, R.; Marotti, L.; Wollstadt, S.; Reigber, A. TOPS Interferometry With TerraSAR-X. *IEEE Trans. Geosci. Remote Sens.* **2012**, *50*, 3179–3188. [CrossRef]

34. Goldstein, R.M.; Werner, C.L. Radar interferogram filtering for geophysical applications. *Geophys. Res. Lett.* **1998**, *25*, 4035–4038. [CrossRef]

35. Hooper, A.J. A statistical-cost approach to unwrapping the phase of InSAR time series. In Proceedings of the Fringe 2009 Workshop, Frascati, Italy, 30 November–4 December 2009.

36. Chen, C.W.; Zebker, H.A. Phase unwrapping for large SAR interferograms: Statistical segmentation and generalized network models. *IEEE Trans. Geosci. Remote Sens.* **2002**, *40*, 1709–1719. [CrossRef]

37. Lazecky, M.; Maghsoudi, Y.; Morishita, Y.; Wright, T.J.; Hooper, A.; Elliott, J.; Hatton, E.; Greenall, N.; Gonzalez, P.J.; Spaans, K.; et al. LiCSAR: An Automatic InSAR Tool for Measuring and Monitoring Tectonic and Volcanic Activities. Manuscript in Preparation.

38. Yu, C.; Li, Z.; Penna, N.T.; Crippa, P. Generic Atmospheric Correction Model for Interferometric Synthetic Aperture Radar Observations. *J. Geophys. Res. Solid Earth* **2018**, *123*, 9202–9222. [CrossRef]

39. Hanssen, R.F. *Radar Interferometry*; Remote Sensing and Digital Image Processing; Springer: Dordrecht, The Netherlands, 2001; Volume 2, ISBN 978-0-7923-6945-5.

40. Bekaert, D.P.S.; Walters, R.J.; Wright, T.J.; Hooper, A.J.; Parker, D.J. Statistical comparison of InSAR tropospheric correction techniques. *Remote Sens. Environ.* **2015**, *170*, 40–47. [CrossRef]

41. Hamlyn, J.; Wright, T.; Walters, R.; Pagli, C.; Sansosti, E.; Casu, F.; Pepe, S.; Edmonds, M.; McCormick Kilbride, B.; Keir, D.; et al. What causes subsidence following the 2011 eruption at Nabro (Eritrea)? *Prog. Earth Planet. Sci.* **2018**, *5*, 31. [CrossRef]

42. Jung, J.; Kim, D.J.; Park, S.E. Correction of atmospheric phase screen in time series InSAR using WRF model for monitoring volcanic activities. *IEEE Trans. Geosci. Remote Sens.* **2014**, *52*, 2678–2689. [CrossRef]

43. Morishita, Y.; Kobayashi, T. Ground Surface Displacement of Kirishima Volcano Group Detected by ALOS-2 InSAR Time Series Analysis and Effect of Atmospheric Noise Reduction. *J. Geod. Soc. Japan* **2018**, *64*, 28–38. [CrossRef]

44. Set I - Atmospheric Model High Resolution 10-Day Forecast (HRES) | ECMWF. Available online: https://www.ecmwf.int/en/forecasts/datasets/set-i (accessed on 27 November 2019).

45. GACOS. Available online: http://ceg-research.ncl.ac.uk/v2/gacos/ (accessed on 27 November 2019).

46. Wang, Q.; Yu, W.; Xu, B.; Wei, G. Assessing the Use of GACOS Products for SBAS-InSAR Deformation Monitoring: A Case in Southern California. *Sensors* **2019**, *19*, 3894. [CrossRef]

47. Wang, X.; Aoki, Y.; Chen, J. Surface deformation of Asama volcano, Japan, detected by time series InSAR combining persistent and distributed scatterers, 2014-2018. *Earth Planets Space* **2019**, *71*, 121. [CrossRef]

48. Shen, L.; Hooper, A.; Elliott, J. A Spatially Varying Scaling Method for InSAR Tropospheric Corrections Using a High-Resolution Weather Model. *J. Geophys. Res. Solid Earth* **2019**, *124*, 4051–4068. [CrossRef]

49. Biggs, J.; Wright, T.; Lu, Z.; Parsons, B. Multi-interferogram method for measuring interseismic deformation: Denali Fault, Alaska. *Geophys. J. Int.* **2007**, *170*, 1165–1179. [CrossRef]

50. López-Quiroz, P.; Doin, M.P.; Tupin, F.; Briole, P.; Nicolas, J.M. Time series analysis of Mexico City subsidence constrained by radar interferometry. *J. Appl. Geophys.* **2009**, *69*, 1–15. [CrossRef]

51. De Zan, F.; Zonno, M.; Lopez-Dekker, P. Phase Inconsistencies and Multiple Scattering in SAR Interferometry. *IEEE Trans. Geosci. Remote Sens.* **2015**, *53*, 6608–6616. [CrossRef]

52. Schmidt, D.A.; Bürgmann, R. Time-dependent land uplift and subsidence in the Santa Clara valley, California, from a large interferometric synthetic aperture radar data set. *J. Geophys. Res. Solid Earth* **2003**, *108*, 1–13. [CrossRef]

53. Doin, M.-P.; Lodge, F.; Guillaso, S.; Jolivet, R.; Lasserre, C.; Ducret, G.; Grandin, R.; Pathier, E.; Pinel, V. Presentation of the small baseline NSBAS processing chain on a case example: The Etna deformation monitoring from 2003 to 2010 using Envisat data. In Proceedings of the Fringe 2011 Workshop, Frascati, Italy, 19–23 September 2011.

54. Efron, B.; Tibshirani, R. Bootstrap Methods for Standard Errors, Confidence Intervals, and Other Measures of Statistical Accuracy. *Stat. Sci.* **1986**, *1*, 54–75. [CrossRef]

55. Hanssen, R.F.; van Leijen, F.J.; van Zwieten, G.J.; Bremmer, C.; Dortland, S.; Kleuskens, M. Validation of existing processing chains in TerraFirma stage 2. Product validation: Validation in the Amsterdam and Alkmaar area Draft version 3. 2008. Available online: https://raw.githubusercontent.com/wiki/yumorishita/LiCSBAS/documents/Hanssen_2008.pdf (accessed on 27 January 2020).

56. Hoffmann, J.; Zebker, H.A.; Galloway, D.L.; Amelung, F. Seasonal subsidence and rebound in Las Vegas Valley, Nevada, observed by synthetic aperture radar interferometry. *Water Resour. Res.* **2001**, *37*, 1551–1566. [CrossRef]

57. Bell, J.W.; Amelung, F.; Ferretti, A.; Bianchi, M.; Novali, F. Permanent scatterer InSAR reveals seasonal and long-term aquifer-system response to groundwater pumping and artificial recharge. *Water Resour. Res.* **2008**, *44*. [CrossRef]

58. Ozawa, S.; Nishimura, T.; Suito, H.; Kobayashi, T.; Tobita, M.; Imakiire, T. Coseismic and postseismic slip of the 2011 magnitude-9 Tohoku-Oki earthquake. *Nature* **2011**, *475*, 373–376. [CrossRef]

59. Suito, H. Current Status of Postseismic Deformation Following the 2011 Tohoku-Oki Earthquake. *J. Disaster Res.* **2018**, *13*, 503–510. [CrossRef]

60. Geospatial Information Authority of Japan. Crustal Movements in the Tohoku District. *Rep. Coord. Comm. Earthq. Predict.* **2018**, *100*, 56–68.

61. Liang, C.; Agram, P.; Simons, M.; Fielding, E.J. Ionospheric Correction of InSAR Time Series Analysis of C-band Sentinel-1 TOPS Data. *IEEE Trans. Geosci. Remote Sens.* **2019**, *57*, 6755–6773. [CrossRef]

62. Weiss, J.R.; Walters, R.J.; Morishita, Y.; Wright, T.J.; Lazecky, M.; Wang, H.; Hussain, E.; Hooper, A.J.; Elliott, J.R.; González, P.J.; et al. Plate-scale measurements of interseismic velocity and strain from Sentinel-1 InSAR and GNSS data. Manuscript in Preparation.

63. Zhang, J.; Bock, Y.; Johnson, H.; Fang, P.; Williams, S.; Genrich, J.; Wdowinski, S.; Behr, J. Southern California permanent GPS geodetic array: Error analysis of daily position estimates and site velocities. *J. Geophys. Res. Solid Earth* **1997**, *102*, 18035–18055. [CrossRef]

64. Aoki, S. Land Sibsidence in Niigata. In Proceedings of the Anaheim Symposium, Anaheim, CA, USA, 13–17 December 1976; pp. 105–112.

65. Niigata Prefecture Ground Subsidence In the Niigata Plain. Available online: http://npdas.pref.niigata.lg.jp/kankyotaisaku/5c85f40531a5c.pdf (accessed on 27 November 2019).

66. Kanto Bureau of International Trade and Industry. *Report for Rationalization of Ground Water Use in Ojiya Area in Niigata Prefecture (Edition for Hydrological Analysis)*; Kanto Bureau of International Trade and Industry: Tokyo, Japan, 1994.

67. Sato, H.P.; Abe, K.; Ootaki, O. GPS-measured land subsidence in Ojiya City, Niigata Prefecture, Japan. *Eng. Geol.* **2003**, *67*, 379–390. [CrossRef]

68. Chaussard, E.; Bürgmann, R.; Shirzaei, M.; Fielding, E.J.; Baker, B. Predictability of hydraulic head changes and characterization of aquifer-system and fault properties from InSAR-derived ground deformation. *J. Geophys. Res. Solid Earth* **2014**, *119*, 6572–6590. [CrossRef]

69. Morishita, Y.; Hanssen, R.F. Deformation Parameter Estimation in Low Coherence Areas Using a Multisatellite InSAR Approach. *IEEE Trans. Geosci. Remote Sens.* **2015**, *53*, 4275–4283. [CrossRef]

70. Rocca, F. Modeling interferogram stacks. *IEEE Trans. Geosci. Remote Sens.* **2007**, *45*, 3289–3299. [CrossRef]

71. Zebker, H.A.; Villasenor, J. Decorrelation in Inteferometric Radar Echoes. *IEEE Trans. Geosci. Remote Sens.* **1992**, *30*, 950–959. [CrossRef]

72. Morishita, Y.; Hanssen, R.F. Temporal decorrelation in L-, C-, and X-band satellite radar interferometry for pasture on drained peat soils. *IEEE Trans. Geosci. Remote Sens.* **2015**, *53*, 1096–1104. [CrossRef]